Wind and Temperature Oscillations Generated by Wave–Turbulence Interactions in the Stably Stratified Boundary Layer

Citation	Sun, J., Mahrt, L., Nappo, C., & Lenschow, D. H. (2015). Wind and Temperature Oscillations Generated by Wave-Turbulence Interactions in the Stably Stratified Boundary Layer. Journal of the Atmospheric Sciences, 72(4), 1484-1503. doi:10.1175/JAS-D-14-0129.1
DOI	10.1175/JAS-D-14-0129.1
Publisher	American Meteorological Society
Version	Version of Record
Terms of Use	http://cdss.library.oregonstate.edu/sa-termsofuse

Wind and Temperature Oscillations Generated by Wave–Turbulence Interactions in the Stably Stratified Boundary Layer

JIELUN SUN

National Center for Atmospheric Research, Boulder, Colorado*

LARRY MAHRT

Oregon State University, Corvallis, Oregon

CARMEN NAPPO

CJN Research Meteorology, Knoxville, Tennessee

DONALD H. LENSCHOW

National Center for Atmospheric Research, Boulder, Colorado*

(Manuscript received 30 April 2014, in final form 17 November 2014)

ABSTRACT

The authors investigate atmospheric internal gravity waves (IGWs): their generation and induction of global intermittent turbulence in the nocturnal stable atmospheric boundary layer based on the new concept of turbulence generation discussed in a prior paper by Sun et al. The IGWs are generated by air lifted by convergence forced by the colliding background flow and cold currents near the ground. The buoyancy-forced IGWs enhance wind speed at the wind speed wave crests such that the bulk shear instability generates large coherent eddies, which augment local turbulent mixing and vertically redistribute momentum and heat. The periodically enhanced turbulent mixing, in turn, modifies the air temperature and flow oscillations of the original IGWs. These turbulence-forced oscillations (TFOs) resemble waves and coherently transport momentum and sensible heat. The observed momentum and sensible heat fluxes at the IGW frequency, which are due to either the buoyancy-forced IGWs themselves or the TFOs, are larger than turbulent fluxes near the surface. The IGWs enhance not only the bulk shear at the wave crests, but also local shear over the wind speed troughs of the surface IGWs. Temporal and spatial variations of turbulent mixing as a result of this wave-induced turbulent mixing change the mean airflow and the shape of the IGWs.

1. Introduction

Nocturnal stable boundary layers (NBL) typically contain wavelike motions. One example is the buoyancy-forced internal gravity wave (IGW). Most documented IGW characteristics are based on the linear gravity wave theory, with the assumption that the wave amplitude is much smaller than the background-flow variation (Nappo 2012). One of the unique characteristics of IGWs is their dispersion relationship; that is, IGWs can travel and transport energy at speeds different from the background wind. In addition, linear IGWs transport momentum but not heat, as horizontal velocity oscillations are 180° and temperature oscillations are 90° out of phase with vertical velocity oscillations. Fundamentally, buoyancy-forced IGWs are initiated by air displacement in a stably stratified environment, which can be generated by, for example, 1) topography (e.g., Chimonas and Nappo 1989; Smith 1989; Belcher and Wood 1996; Rees et al. 2000, 2001; Yagüe et al. 2001; Brown et al. 2003; Teixeira and Miranda 2004; Vosper and Brown 2007; Chemel et al. 2009) and 2) disturbed streamlines related to convergence

* The National Center for Atmospheric Research is sponsored by the National Science Foundation.

Corresponding author address: Jielun Sun, National Center for Atmospheric Research, 3450 Mitchell Lane, Boulder, CO 80307. E-mail: jsun@ucar.edu

DOI: 10.1175/JAS-D-14-0129.1

zones between background flow and density currents from downdrafts of convective systems (e.g., Curry and Murty 1974; Balachandran 1980; Chimonas and Nappo 1987) and downslope drainage flows (e.g., Jordan 1972; Rees and Mobbs 1988; Balsley et al. 2002; Sun et al. 2002; Mahrt 2010; Viana et al. 2010). Because of the rapid decrease of the atmospheric density with height, especially under the influence of longwave radiative cooling of the ground at night, IGWs are sometimes ducted within the lower atmosphere for many cycles (e.g., Rees and Rottman 1994; Chimonas 2002; Fritts et al. 2003; Meillier et al. 2008).

Wavelike motions in the NBL are also likely initiated by shear instability; these motions are called vorticity waves by Carpenter et al. (2013) based on their generation mechanism. Atmospheric conditions that may trigger wavelike motions have been extensively investigated (e.g., Hardy et al. 1973; Einaudi and Finnigan 1981; Finnigan and Einaudi 1981; Finnigan et al. 1984; Gossard et al. 1985; Einaudi et al. 1989; Fitzjarrald and Moore 1990; Chilson et al. 1997; Lee et al. 1997; Blumen et al. 2001; Hu et al. 2002; Newsom and Banta 2003; Finnigan et al. 2009; Belcher et al. 2012). In the literature, both buoyancy-forced and shear instability generated periodic motions are commonly called waves.

In addition to waves, the NBL is also characterized by global intermittent turbulence (Mahrt 1989). Turbulence intermittency has been investigated through both observations (e.g., Kunkel and Walters 1982; Nappo 1991; Sun et al. 2002; Acevedo and Fitzjarrald 2003; van de Wiel et al. 2003; Doran 2004; Sun et al. 2004; Banta et al. 2007; Vindel and Yagüe 2011) and numerical modeling (e.g., Costa et al. 2011; Zhou and Chow 2012). Intermittent turbulence and waves are often connected. Einaudi and Finnigan (1981), Finnigan and Einaudi (1981), and Einaudi and Finnigan (1993) studied wave–turbulence interactions by decomposing observations into mean, turbulence, and wave components. Wave–turbulence interactions have been theoretically investigated at wave critical levels, where wind speed equals wave phase speed (e.g., Geller et al. 1975; Nappo and Chimonas 1992; Dörnbrack and Nappo 1997; Tjernström et al. 2009). Waves with large amplitudes can also lead to turbulence through nonlinearity (e.g., Staquet and Sommeria 2002; Staquet 2004). However, most studies focus on wave breaking, with little discussion on how turbulence affects wave characteristics.

Intermittent turbulence and gravity waves in the stable atmosphere have long been obstacles for numerical modeling, and understanding wave–turbulence interactions is particularly challenging (e.g., Thorpe 1987). Wave–turbulence interactions are highly nonlinear and depend on both background flow and wave disturbances. However, we find that there is a common IGW generation and wave–turbulence interaction pattern (section 2), which occurs frequently, whenever the wind is weak [i.e., more than 74% of the time during the 1999 Cooperative Atmosphere–Surface Exchange Study (CASES-99) conducted in Kansas, United States (section 3)]. In other words, although wave–turbulence interaction processes are case dependent in terms of both location and strength of turbulence relative to IGWs, as well as the feedback of turbulence on IGWs, the turbulence generation processes are similar and can be explained using the concept developed in Sun et al. (2012, hereafter S12), as described in more detail in the next section. We describe the physical processes through the analysis of two nights: 20 October in detail and 9 October for corroboration. As a result of the surface influence on turbulence generation, wave–turbulence interactions, and varying background wind on which the wave motions are imposed, the observed wind oscillations may not resemble the familiar sinusoidal waves with approximately constant amplitude and wavelength that are commonly investigated in the literature. Nonetheless, wave motions with varying amplitudes and wavelengths are common and are investigated here. We focus on the observed turbulence generation and the role of turbulence in forcing wind and temperature oscillations as a result of waves in the NBL near the ground. Comparison between these two individual cases and the statistical results in S12 can shed light on the general turbulence generation processes in the NBL.

Numerous researchers have used the CASES-99 dataset for investigating stable boundary layers, including turbulence intermittency (e.g., Coulter and Doran 2002; Ha et al. 2007), but mainly focusing on general temporal and spatial patterns of intermittent turbulence. Some of them also incorporated one of the nights used in this study, but for different scientific problems (e.g., Balsley et al. 2002; Banta et al. 2007). In this study, we analyze observations in detail to examine wave generation (section 4) and characteristic structure (section 5), how the waves modify the background wind and lead to intermittent turbulence, and how wave–turbulence interactions generate wind and temperature oscillations that modify IGWs and lead to turbulence-forced oscillations (section 6). Conclusions are in section 7.

2. Theoretical framework of wave–turbulence interactions

S12 found that at a given height, nocturnal turbulent mixing can mainly be divided into weak and strong regimes depending on the relationship between turbulence strength and wind speed, where turbulence

strength can be either the standard deviation of horizontal wind speed or vertical wind component or the square root of turbulent kinetic energy. They also found that turbulence in the strong regime, which corresponds to the near-neutral regime, was generated by the bulk shear V/z, where V is the wind speed at height z, and the turbulence strength increased linearly with V at a given z. The large coherent eddies that scale with z contributed most to the strong turbulent mixing. As a result of the efficient large-eddy mixing, the vertical temperature gradient near the ground was reduced to nearly zero. In contrast, relatively weak turbulence in the weak turbulence regime was generated by local shear instability with a vertical scale less than z. Because of a lack of large coherent eddies that reach down to the ground, stable stratification was prominent in the weak turbulence regime. On average, the two regimes at a given z were separated by a threshold wind speed V_s. The plot showing the transition of turbulence strength as a function of V between the two regimes resembles a hockey stick, analogous to the hockey-stick graph of Mann et al. (1999). Therefore we call this dramatic transition in turbulence as a function of a critical shear the hockey-stick transition (HOST). HOST challenges the universality of the dependence of turbulent momentum flux on $\partial V/\partial z$, such as in the Monin–Obukhov similarity theory (MOST), particularly for strong turbulence where the turbulence is observed to relate to V/z.

HOST appears at all nine observation heights over the 60-m observation depth in S12, and the threshold wind speed systematically increases with height. Similar HOST has been found elsewhere (van de Wiel et al. 2012; Mahrt et al. 2013; Martins et al. 2013). Some earlier studies also found this sharp increase of turbulence strength with wind speed (e.g., King et al. 1994; Acevedo and Fitzjarrald 2003). In addition to these two regimes, turbulence that is transported from surrounding areas instead of being generated by bulk or local shear instability associated with the local wind has a different relationship between turbulence strength and wind speed.

We apply HOST to understand the observed wave–turbulence interactions, where the IGWs are generated near the ground and are characterized by an antiphase relationship between the horizontal and vertical wind components (Fig. 1; see section 5 for detailed wave analyses). Because the threshold wind speed that leads to the strong turbulent mixing regime increases with height, the wind speed oscillation near the ground readily exceeds its threshold value compared to the air above. Therefore, the wind speed oscillation of the surface IGWs enables the wind speed to exceed its threshold value at the wind speed maximum of the periodic component of the flow (herein, wave crests), where the bulk shear instability initiates strong turbulent mixing. The deep strong mixing enables large coherent eddies at the wave crests, which transport warm and high-momentum air downward, and cold and low-momentum air upward in the stably stratified layer near the ground. As a result of the vertical redistribution of the air of different temperatures that occurs at the wave crests, the air temperature appears to oscillate at the IGW frequency with a phase angle that varies with height instead of 90° from the wave vertical velocity, as in a linear IGW. Near the ground, the temperature oscillation is in phase with the wind speed of the IGWs; that is, the periodic maximum wind speed and downward motion are associated with the periodically warmer air. The same strong turbulent mixing also redistributes the air of different momenta, enhancing the airspeed near the ground and reducing the airspeed above. The reduced airspeed above may lead to either IGWs with a reduced amplitude in the wind speed oscillation or a reversed wind speed oscillation, which is antiphase with the surface IGWs. These are the turbulence-forced oscillations (TFOs).

The surface IGWs also enhance local shear over the wind speed minimum of the periodic component of the flow (herein, wave troughs) when the airflow is reduced near the ground. The resulting enhanced local shear is elevated above the ground, is smaller than the bulk shear, and generates relatively weak turbulent mixing. Because the elevated turbulent mixing leads to an increase of turbulence with height, it reduces the local mean vertical velocity and enhances the local mean horizontal flow at the wave troughs where the vertical velocity of the IGWs is maximum and the wind speed is minimum (section 6). Consequently the elevated turbulent mixing over the wave troughs can shorten the wave period. Therefore, the IGW-induced turbulent mixing in the two turbulence regimes associated with wave crests and troughs impacts the existing IGW characteristics.

We demonstrate how we can apply the HOST concept to two cases to explain wave–turbulence interactions, where the variation of the turbulence strength is not linearly related to the local shear $\partial V/\partial z$. Through these two cases, we also demonstrate what HOST in S12 is built upon. The observed IGW generation and the consequent wave–turbulence interactions following the above-mentioned physical processes are summarized schematically in Fig. 1.

3. Observations and data processing

The nocturnal data used in this study were collected from a 60-m tower and six 10-m satellite towers (Fig. 2)

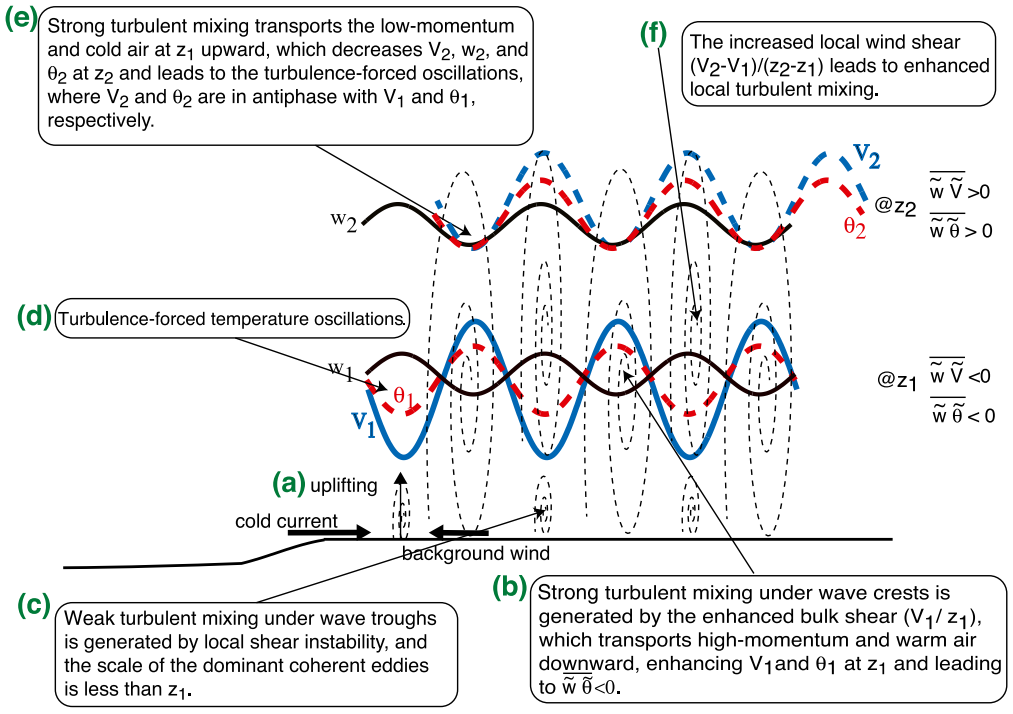

FIG. 1. Schematic cross section of wave–turbulence interactions. (a) IGW generation due to air lifted by convergence between the background flow and a cold current; (b) strong turbulent mixing generated by bulk shear instability at the wave crests of the IGW at z_1; (c) weak turbulent mixing generated by local shear at the wave troughs when V at z_1 is low; (d) θ oscillation at z_1 resulting from downward transport of warm air by the strong turbulence at the wave crests at z_1; (e) V and θ oscillations (i.e. TFOs) at z_2 resulting from the upward transport of cold and low-momentum air by the strong turbulence at the wave crests at z_1; and (f) weak turbulent mixing above the wave troughs at z_1 when V is low at z_1 but higher at z_2. Here, V, w, and θ are the wind speed, the vertical velocity, and the potential temperature, respectively. The tilde represents the oscillation at the IGW frequency.

during CASES-99 (Poulos et al. 2002; Sun et al. 2002, 2013). Six three-dimensional (3D) sonic anemometers (SAs) were installed at 10-, 20-, 30-, 40-, 50-, and 55-m height on the 60-m tower. Two additional SAs were installed at 1.5- and 5-m height on a 10-m tower, which was 10 m east of the 60-m tower to avoid flow distortion from the base of the 60-m tower. The observations referred to in this study as 60-m tower observations actually came from both towers. The lowest SA was moved from 1.5 to 0.5 m starting on 20 October. In addition to the SA data, five levels of prop-vane wind were obtained at 15, 25, 35, and 45 m. The air temperature was measured at 34 levels by thermocouples with a vertical resolution of 1.8 m on the 60-m tower from 2.3 to 58.1 m, and also at 0.23 and 0.63 m on two adjacent poles about 1 m from the 60-m tower. At each satellite station, a wind vane, a 3D SA, a temperature–humidity sensor, and a pressure sensor were installed at 10, 5, 2, and 1.5 m, respectively. The location of the six satellite stations and the calculation of the horizontal pressure gradient were described in Sun et al. (2013). Station 3 was located in a relatively low and wet area compared to the other towers; its measurements may not follow large-scale trends and are not used in this study.

All 12 levels of wind measurements are used in calculating $\partial V/\partial z$, as described in Sun (2011). In brief, the wind speed profile at three measurement levels, including one at z, one below, and one above, are fitted with a log-linear function of z, and local shear is calculated using this locally fitted wind profile. Although $|\partial \mathbf{V}/\partial z| \geq \partial V/\partial z$, where $\partial \mathbf{V}/\partial z$ and $\partial V/\partial z$ represent a vector and a speed shear, respectively, the two differ only when wind speed is weak, as vertical variations of wind direction are eliminated by strong mixing associated with strong winds. We use $\partial V/\partial z$ in this study to focus on contrasts between MOST and HOST in near-neutral conditions (i.e., the strong-wind regime).

Wavelet analysis used in this study is based on the Haar basis, instead of the popular Morlet basis. Although both wavelets can capture periodic motions in

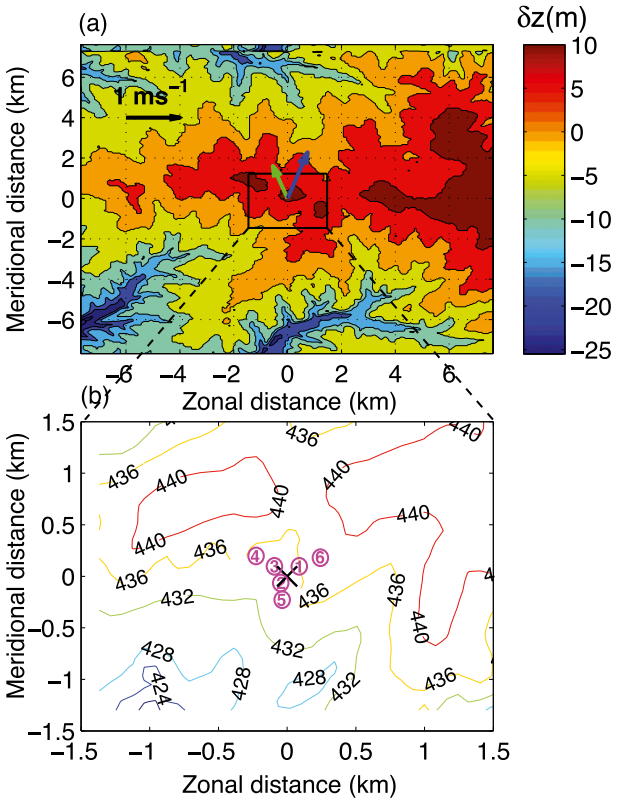

FIG. 2. (a) The elevation variation relative to the area mean around the CASES-99 site and (b) the elevation (m) above sea level around the 60-m tower with the six satellite stations (magenta circles and numbers) and the 60-m tower (black ×). The cold-current vectors, which are approximately the same as the IGW propagation vector, are marked for the 20 Oct (green) and 9 Oct (blue) major events in (a). A 1 m s^{-1} reference vector is plotted at the upper-left corner of (a).

the atmosphere, atmospheric variations do not resemble Haar or Morlet functions. Haar wavelets are simpler and orthogonal, which leads to no ambiguity in interpretation of decomposed variations (Howell and Mahrt 1994; Howell 1995; Howell and Sun 1999).

The wind speed at 55 m was stronger than 10 m s^{-1} for a significant fraction of 6 nights (7, 11, 13, 15, 17, and 25 October), less than 7 m s^{-1} for the night of 26 October, and between these two values for the remaining 20 nights during CASES-99. The wind at 55 m for the two nights analyzed in this study is relatively weak (i.e., less than 10 m s^{-1}). This is the case for 74% of the nights when wave–turbulence interactions were observed. On the night of 20 October, a weak and broad high pressure system was centered in northern Utah, and a small high pressure system was centered in northwestern Texas. The wind changed gradually from weak northerly to southerly during the night as a low pressure trough moved slowly southward to northwestern Kansas. On the night of 9 October, a high pressure system was centered in southwestern Colorado and northwestern New Mexico and slightly strengthened eastward toward the morning. The wind remained northeasterly to northerly throughout the night.

The dates are labeled in UTC time. For example, the time period of the night of 19 October and the early morning of 20 October is from 0000 to 1200 UTC 20 October; therefore, we label this night as 20 October. The local standard time is 6 h behind UTC.

4. Wave generation and characteristics

IGWs have been observed to be associated with density currents either from downslope wind (e.g., Jordan 1972; Nappo et al. 2008; Viana et al. 2010) or thunderstorms (e.g., Curry and Murty 1974; Balachandran 1980). Both processes can provide the uplift required for IGW generation in a stably stratified environment. Here, we demonstrate that the density current for this kind of IGW generation can be on a much smaller scale and shallower than the 60-m observation layer. We illustrate that buoyancy-forced IGWs are due to convergence between background wind and cold currents near the surface.

Wavelike motions lasted throughout the night of 20 October at all the stations (Fig. 3b). The relatively clean wavelike motions at the lowest SA level (i.e., 0.5 m) started right after the wind speed decreased to near zero around 0200 UTC (marked "3" in Fig. 4a) as the meridional wind speed suddenly changed from northerly to southerly for about 15 min in the bottom half of the 60-m observation layer; this temporal change of air motion was also evident at all the satellite stations (Figs. 3c, 4b). The wind in the upper half of the 60-m layer was not affected by this change and varied gradually from northerly at the beginning of the night to southerly toward the end of the night, which is consistent with the synoptic situation. At the time of the sudden wind direction change, the temperature decreased sharply (Figs. 4e, 5d). The temperature reduction and the water vapor specific humidity perturbation decreased with height (Fig. 5), indicating the arrival of a cold current near the ground. The wave development is evident in the sharp enhancement of the vertical velocity (Fig. 5c). The increasing amplitude of the vertical velocity with height is due to the general increase of the vertical velocity with height near the ground and the decreasing influence of turbulence on waves with height (more in section 6). The initial changes of the wind direction and air temperature are the most abrupt among all the observed variables and are used to estimate the speed and direction of the cold current based on the time differences of those

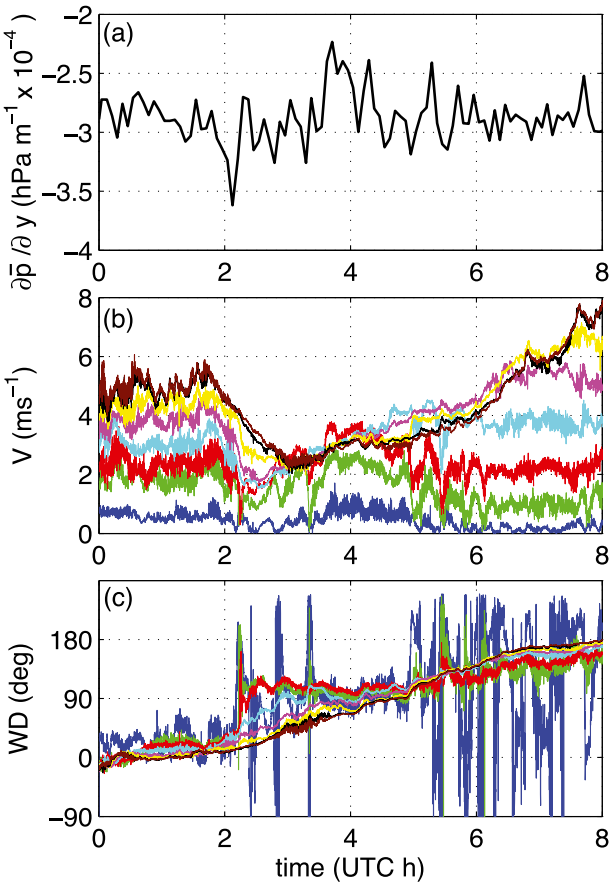

FIG. 3. Wave–turbulence interactions on the night of 20 Oct, where the surface IGW generation is associated with convergence between the background flow and the cold current around 0212 UTC resulting in the meridional pressure gradient spike and the wind direction change in the bottom half of the 60-m observation layer. Shown here are the time series of (a) meridional pressure gradient, (b) wind speed, and (c) wind direction on the night of 20 Oct. The 5-min-averaged pressures are used in (a); 0.2-s^{-1} data are used in (b) and (c). The waves are analyzed in Fig. 10.

sudden changes at the stations. Principally, the method is the same as the beam-steering method (e.g., Nappo 2012). We find that the cold air propagated at 0.8 m s^{-1} and was from 161° ± 5° (represented by the light green vector in Fig. 2a). Using the pressure measurements at three stations and applying the beam-steering method, the derived wave propagation speed and direction are approximately the same as the cold current within the uncertainty of the beam-steering method and the observed arrival time at each station.

We also find that the arrival of the cold current is closely related to a negative horizontal pressure gradient spike. When the northward-moving cold current reached the southernmost station, the local pressure increased, resulting in a sharp decrease of the meridional pressure gradient (Figs. 3a, 4f). As the cold current passed through the other stations, the horizontal pressure gradient returned to its weaker negative value. Using the observed pressures and air temperature at stations 5 and 2, which are at about the same longitude and altitude, we estimate the depth of the cold current using the hydrostatic relationship described in Sun et al. (2013) to be 35 m. This compares reasonably well with the highest level that the sharp temperature decrease was detected by the thermocouples (Fig. 5d), as well as the wind direction oscillation by the SAs (Fig. 5b). This agreement suggests that the sudden meridional pressure gradient spike is indeed associated with the arrival of the cold current, even though the nonhydrostatic pressure may also contribute to the pressure change at the arrival of the cold current.

The terrain at the CASES-99 site is, in general, tilted slightly downward toward the west with an elevation change of less than 10 m across 20 km in the east–west direction (Fig. 2). In addition, there are shallow gullies north and south of the site. Because of the relatively weak wind throughout almost the entire night, development of drainage flows is inevitable (e.g., Soler et al. 2002; Sun and De Wekker 2012), which is evident from the wind direction down the southwestern terrain slope prior to the arrival of the cold current. After the arrival of the cold current, the flow in the bottom half of the 60-m layer was initially influenced by the northward cold current for about 15 min and later by the drainage flow toward the southwest until 0500 UTC, when the entire 60-m layer was under the influence of the synoptic flow.

We had no tower observations in the gully south of the site, so we can only speculate on the origin of the cold current based on the observational study of a gully southwest of the 60-m tower during CASES-99 by Soler et al. (2002), the large-eddy simulation by Zhou and Chow (2014) using the CASES-99 topography but for a different night, and also a different observational study by Lenschow et al. (1979). Both the drainage flow down the southwestern terrain slope and the synoptic flow over the cold gully south of the site could enhance the shear over the gully. Subsequently, the shear-generated turbulent mixing could transport the cold air out of the cold pool, replacing it with warm overlaying air. The increased hydrostatic pressure of the cold air may add to the synoptic pressure gradient, which could ''push'' the cold air away from the gully toward the tower. The observed relationship between the negative meridional pressure gradient and the southerly wind based on the entire nocturnal CASES-99 dataset (Sun et al. 2013) adds credibility to this speculation.

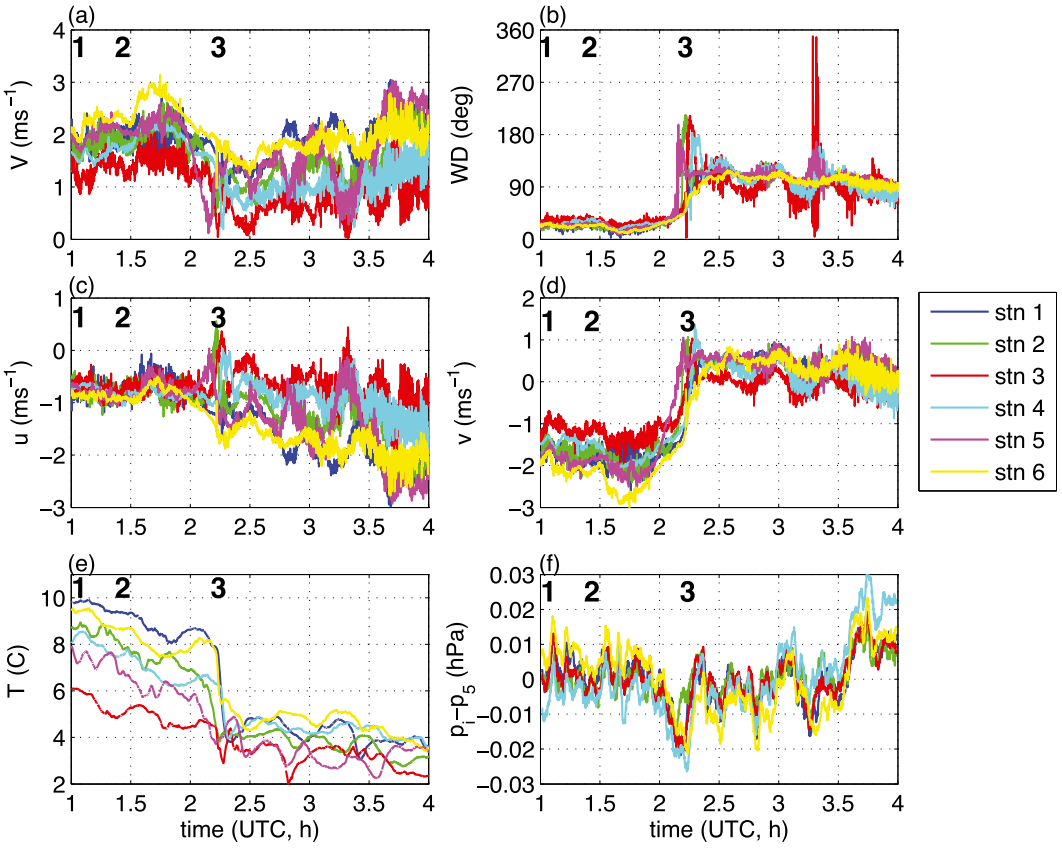

FIG. 4. Wave–turbulence interactions on the night of 20 Oct measured at the six satellite stations, indicating the correlation between the sharp temperature decrease, the wind direction change, the wind speed change, the meridional wind change, and the pressure change relative to the southernmost station around 0200 UTC. Because of the temporal variation of the background flow and wave–turbulence interactions, wind oscillations may not be obvious here but are visible when zoomed in, as in Figs. 9 and 11, or in wavelet analysis when the IGW motions are effectively separated from the other motions, as in Fig. 10. Shown are the time series of (a) 5-m wind speed, (b) 5-m wind direction, (c) 5-m zonal wind, (d) 5-m meridional wind, (e) 2-m air temperature at the six stations, and (f) linearly detrended pressure difference between station i (i = 1–6) and station 5 (i = 5) during the period of 0100–0400 UTC 20 Oct. The data are plotted here at 0.2 s^{-1}. The boldface black numbers 1–3 mark the cold-current events.

Similar wavelike motions occurred on the night of 9 October (Fig. 6). Significant cold currents were observed around 1000 UTC. Based on the sharp temperature decrease across the observation domain, such as the one marked "3" in Figs. 7e and 8d, the wave traveled at 1.3 m s^{-1} from 198° ± 5° (represented by the dark blue vector in Fig. 2a). Again the vertical decreases of the wind speed, potential temperature, and water vapor specific humidity oscillation amplitudes in Fig. 8 suggest that the wavelike event was also initiated near the ground. Balsley et al. (2002) found four cases of cold currents up the gully southwest of the CASES-99 site; the 9 October event is one of them. Using the observed pressures and temperatures at stations 2 and 5, the estimated height of the cold current for this event is about 65 m, which is again consistent with the temperature decrease and the wind oscillation at the highest observation level on the 60-m tower (Fig. 8). We speculate that the relatively deep cold current here is due to the moderate background wind compared to that on 20 October, which causes the cold air to mix farther upward and deepens the cold pool southeast of the site.

Similar to the above major cold currents associated with the gullies surrounding the site, wave motions are also triggered by even weaker drainage flows, which occurred prior to the major cold currents investigated above, such as the events marked "1" and "2" for each night (Figs. 4, 5, 7, 8). In contrast to the above-mentioned major cold currents, the wind at the time of these minor cold currents is from the north-northeast (Figs. 4b, 7b), and the wind direction change at the arrival of the minor cold currents is barely noticeable because of the moderate background wind. A close examination indicates that the wind speed decrease at the time of the minor events is

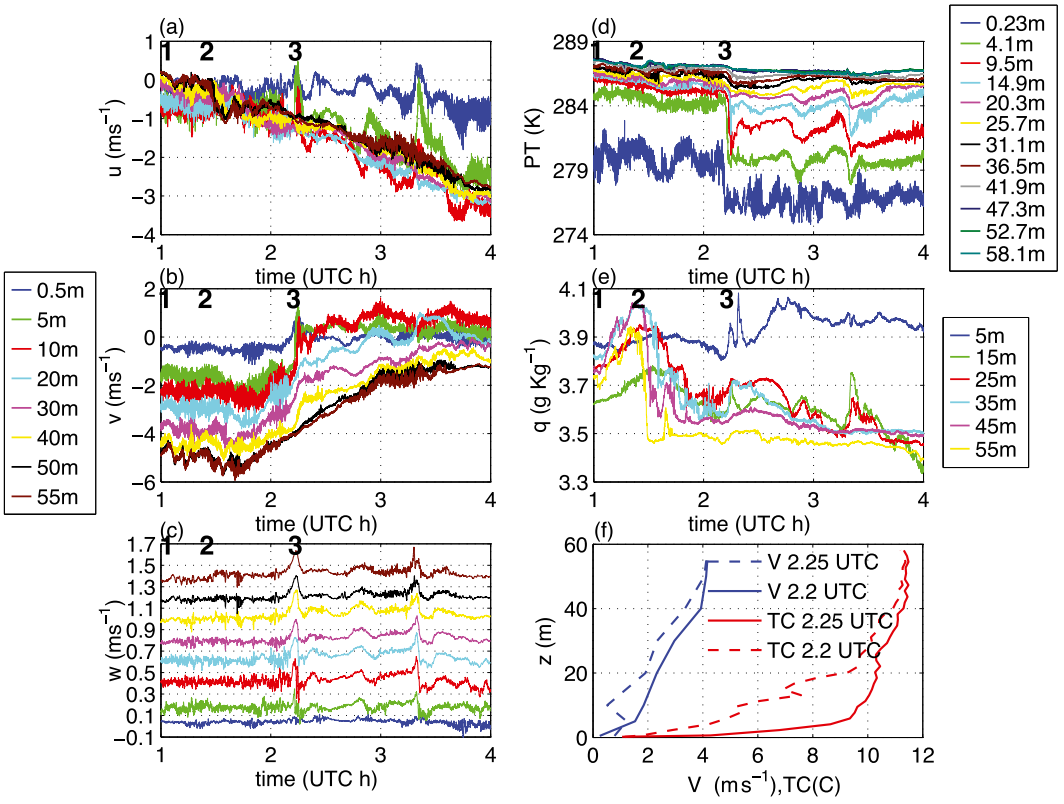

FIG. 5. Vertical variations of the wave–turbulence interactions on the night of 20 Oct indicating the depth of the cold current, the vertical propagation of the IGWs, and the mini LLJ as a result of the strong turbulent mixing at the beginning of the IGWs [dashed lines in (f)] compared to the ones before the arrival of the cold current. The wavelet analysis of wind is in Fig. 10. Here (a) u, (b) v, (c) w, (d) PT, (e) q, and (f) V and TC represent zonal, meridional, and vertical winds, potential temperature, water vapor specific humidity, wind speed, and thermocouple temperature, respectively. The w value at the heights above the lowest SA is shifted by 0.3 m s^{-1} from the level below for easy viewing. The data used here are sampled at 0.2 s^{-1}. The boldface black numbers 1–3 mark the cold current events.

mainly due to a small decrease in the westerly wind component u, while the meridional wind component v change is relatively small, as v is much stronger than u (Fig. 9). These observations suggest that these minor cold currents are associated with drainage flows down the southwestward slope. For event 2 on the night of 20 October, the high humidity peak in Fig. 5e is associated with relatively strong vertical mixing in the middle of the 60-m layer, which could be advected from the stronger vertical mixing upstream of the 60-m tower as the underlying 60-m layer is stabilized by the minor cold current. Both strong and weak cold currents generated a similar range of wave frequencies. Although the minor cold currents individually have less impact, they may be much more common than the major cold currents.

5. Internal gravity waves

We apply the Haar wavelet analysis described in Howell and Sun (1999) to the time series of the air motion to examine the time–frequency distribution of the wavelike motions relative to the arrival of the cold currents each night. The wavelet analysis is performed on the vertical velocity w and the wind speed V along the wind direction averaged between 0100 and 0400 UTC 20 October and between 0500 and 1200 UTC 9 October with a moving time segment about 2 h in length at every 8 s along the time series. On both nights, the kinetic energy, KE = $0.5(V^2 + w^2)$, has a periodic maximum at a wave period of about T_w =20 min at the lowest SA level (Fig. 10), and its variation is dominated by V. The magnitude of the KE oscillation at the time period of T_w increases significantly after the arrival of the major cold current each night.

Based on comparison between the linear inviscid theory and the observed nonlinear waves, Einaudi and Finnigan (1993) suggest that the linear wave theory approximately captures the basic physics for observed wave periods and wavelengths. Based on the linear wave theory, buoyancy can only support IGWs with

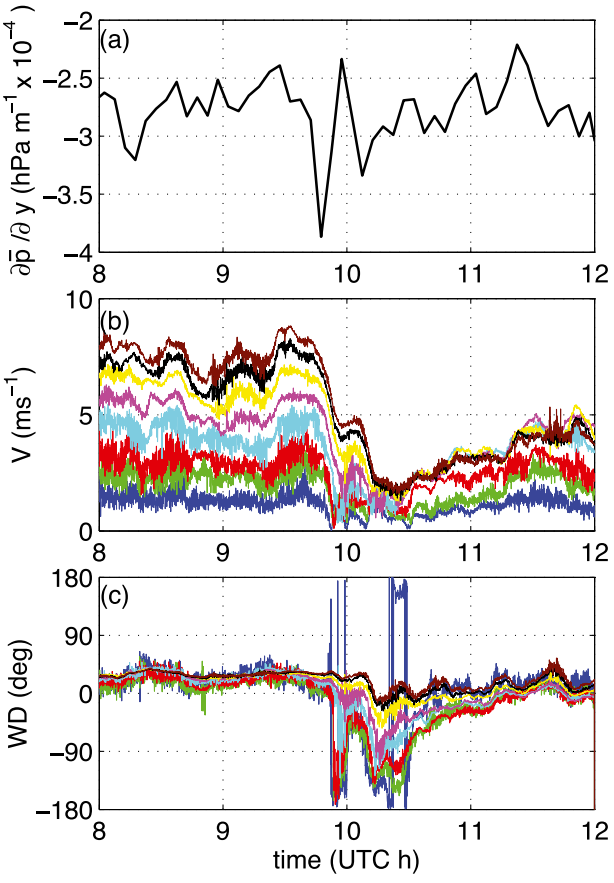

FIG. 6. Wave–turbulence interactions on the night of 9 Oct, where the surface IGW generation is associated with convergence between the background flow and the cold current around 0948 UTC, resulting in the meridional pressure gradient spike and the wind direction change. The labels are as in Fig. 3. The waves are analyzed in Fig. 10.

frequencies between the Coriolis frequency f at the low frequency end and the Brunt–Väisälä frequency $N = [(g/\theta_0)(\partial\theta/\partial z)]^{1/2}$ at the high-frequency end, where θ_0 is the reference potential temperature (e.g., Gossard and Hooke 1975). The estimated N is about 0.15 s^{-1} on 20 October and 0.1 s^{-1} on 9 October. Thus, using T_w as the estimated wave period, the observed wave frequency is indeed less than the observed linear wave frequency limit N for both nights.

The appearance of the simultaneous horizontal wind change and the upward vertical motion on both nights—both the dramatic meridional wind change at the arrival of the major cold currents and the minor zonal wind change at the arrival of the minor cold currents—suggests that the wave motions are IGWs generated by the air lifted by the collision between the cold currents and the background flows (Fig. 1). The resulting minimum wind speed at the arrival of each cold current, especially the major ones, reduces the turbulent mixing and upward cold-air transport, which temporarily helps maintain the vertical temperature gradient that is enforced by the arrival of the cold current near the ground.

The horizontal and vertical wave oscillations are related through the mass continuity equation. By definition, the vertical wavenumber of IGWs has to be real. Therefore, the horizontal and vertical wave components (expressed with tildes) are related through the wavenumbers in the horizontal (k) and vertical (m) directions as

$$\tilde{V} = -\frac{m}{k}\tilde{w}. \tag{1}$$

Equation (1) indicates that for positive m and k, a maximum in $\tilde{V}$ corresponds to a minimum in $\tilde{w}$, implying that $\tilde{V}$ and $\tilde{w}$ should be 180° out of phase or antiphase for a two-dimensional IGW (Nappo 2012). The observed apparent antiphase relationship between $\tilde{V}$ and $\tilde{w}$ (Figs. 9, 11) further suggests that the observed wave motions are IGWs. The phase relationship between $\tilde{V}$ and $\tilde{w}$ also suggests the interchange between potential and kinetic energy once an air parcel is lifted. This energy exchange gives rise to the wind speed oscillations.

We calculate momentum and sensible heat fluxes associated with IGWs using the Haar wavelet analysis. We first examine the cospectra Co[w, V] between w and V and the cospectra Co[w, θ] between w and θ from 0100 to 0600 UTC 20 October and from 0800 to 1200 UTC 9 October. For both nights, the magnitudes of both cospectra peak at a period of about 20 min, and are uniformly small at the higher-frequency end (Fig. 12). Based on the observed Co[w, V], we define wave momentum flux $\tilde{w}\tilde{V}$ (where the overbar represents an integral over a range of time scales) as Co[w, V] integrated over the time scale from 1 to 60 min to include the wave frequency, and turbulent momentum flux $\overline{w'V'}$ as Co[w, V] integrated over time scales smaller than 1 min to exclude the wave frequency. Based on the variation of Co[w, V] with the frequency, it is not surprising that the magnitude of $\tilde{w}\tilde{V}$ is much larger than that of $\overline{w'V'}$ on both nights, which has also been observed by Finnigan and Einaudi (1981). Similarly, the magnitude of the wave sensible heat flux $\tilde{w}\tilde{\theta}$ is much larger than that of the turbulent sensible heat flux $\overline{w'\theta'}$ during the wave period on both nights. In addition, both $\tilde{w}\tilde{V}$ and $\tilde{w}\tilde{\theta}$ are negative at the lowest SA level on both nights, which further confirms the antiphase relationship between $\tilde{w}$ and $\tilde{V}$. However, both wave fluxes are positive at 5 and 10 m on 20 October and only at 5 m on 9 October; they switch back to negative values above the positive flux layer on 9 October but remain positive and gradually decrease to near zero on 20 October. The nonzero wave heat fluxes suggest that the IGWs are influenced by turbulence and nonlinearity, as linear

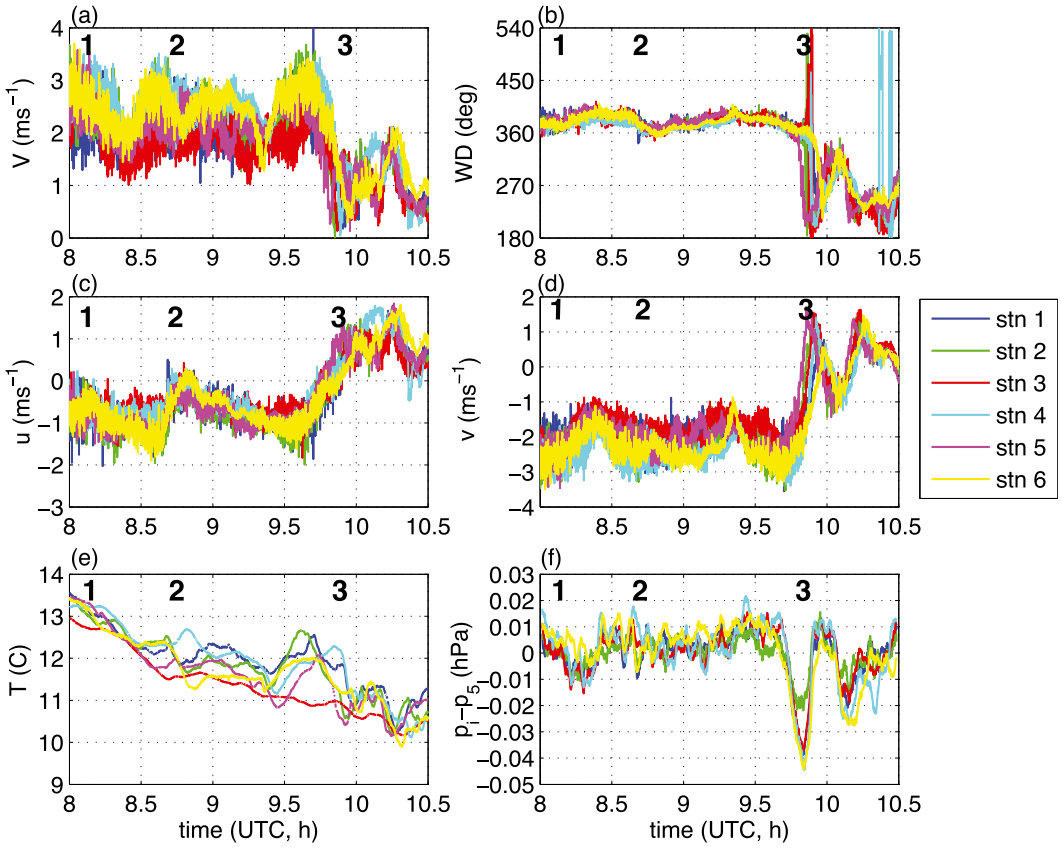

FIG. 7. The wave–turbulence interactions on the night of 9 Oct measured at the six satellite stations. The labels are as in Fig. 4.

IGWs transport momentum but not heat (e.g., Nappo 2012).

We now investigate the time–frequency distribution of Co[w, V] and Co[w, θ] around the wave period (i.e., Co[$\tilde{w}$, $\tilde{V}$] and Co[$\tilde{w}$, $\tilde{\theta}$]) using the same Haar wavelet analysis method as for the KE analysis described above to examine the temporal variation of Co[$\tilde{w}$, $\tilde{V}$] and Co[$\tilde{w}$, $\tilde{\theta}$] relative to the arrival of the cold currents. We concentrate on the bottom three SA levels to illustrate interactions between the IGW and turbulence for the night of 20 October (Fig. 13). Similar physical processes occur above 10 m. We find that at 0.5 m, Co[$\tilde{w}$, $\tilde{V}$] shifts from dominantly positive to negative after the arrival of the cold current. Comparison between the KE in Fig. 10 and Co[w, V] in Fig. 13 indicates that, at 0.5 m, negative maxima of Co[$\tilde{w}$, $\tilde{V}$] occur at the IGW wave crests. In contrast, at 5 m, positive maxima of Co[$\tilde{w}$, $\tilde{V}$] occur at the IGW wave crests (i.e., the Co[$\tilde{w}$, $\tilde{V}$] oscillation reverses between 0.5 and 5 m). Co[$\tilde{w}$, $\tilde{V}$] at 10 m is similar to that at 5 m. A simplified schematic of the above-described oscillations is given in Fig. 1.

The negative maxima of Co[$\tilde{w}$, $\tilde{\theta}$] at 0.5 m are also associated with the wave crests, and the oscillation of Co[$\tilde{w}$, $\tilde{\theta}$] at 5 and 10 m is antiphase with that at 0.5 m (Fig. 13). The appearance of the enhanced Co[$\tilde{w}$, $\tilde{\theta}$] oscillation at time scales other than the wave frequency and prior to the arrival of the cold current is a by-product of the decomposition of the sharp decrease in the air temperature at the arrival of the cold current by the Haar spectral analysis (Fig. 5d), which is a general characteristic of spectral analysis. In other words, the sharp temperature change results in a spread-out response in both the frequency and time domains (Howell and Mahrt 1994; Howell 1995). This artificial phenomenon related to the sharp temperature change in Fig. 13 does not significantly affect the time-integrated sensible heat fluxes over the 5-h period in Fig. 12. The time–frequency distributions of Co[w, V] and Co[w, θ] on the night of 9 October are similar to those on 20 October (not shown). The significant difference between 20 and 9 October is that the depth of the positive Co[$\tilde{w}$, $\tilde{V}$] and Co[$\tilde{w}$, $\tilde{\theta}$] layer is relatively thin on the night of 9 October compared to the night of 20 October, and the periodic negative Co[$\tilde{w}$, $\tilde{V}$] and Co[$\tilde{w}$, $\tilde{\theta}$] maxima at 10 m and above on the night of 9 October are unaffected by the turbulent mixing below.

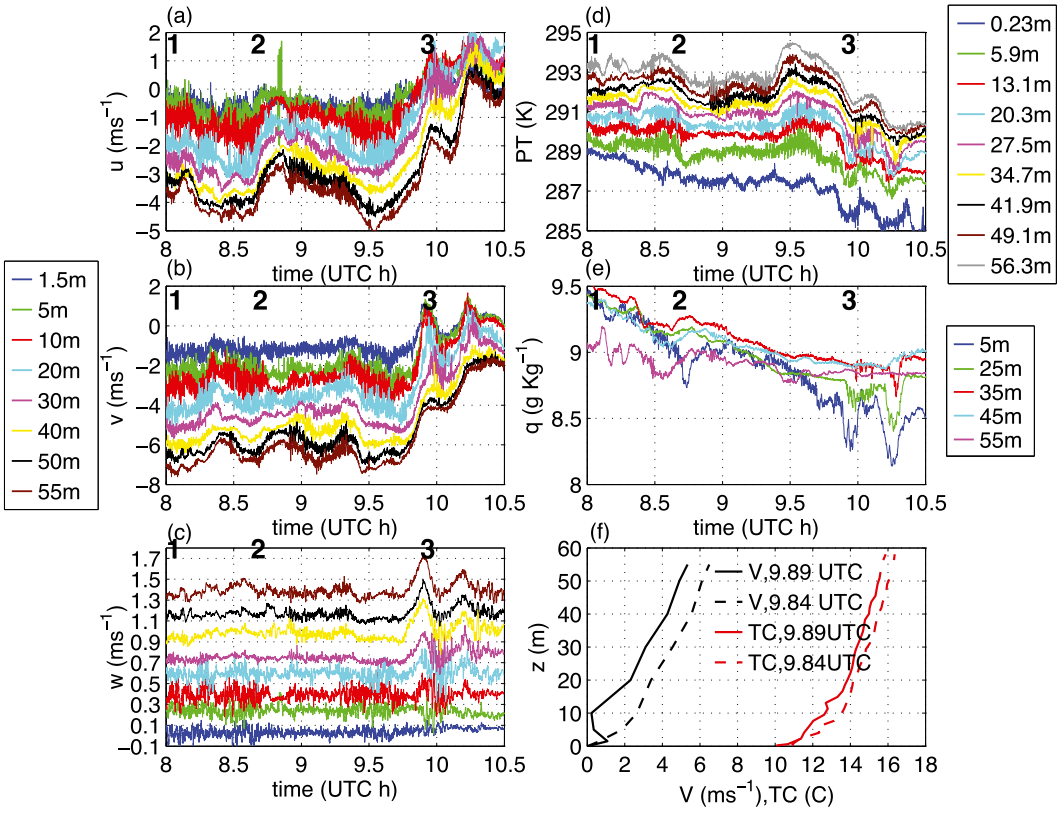

FIG. 8. Cross sections of the wave–turbulence interactions on the night of 9 Oct. The labels are as in Fig. 5.

6. Wave–turbulence interactions

Guided by the observation of the two turbulence regimes in S12, we analyze wave–turbulence interactions by focusing on the wave crests where strong turbulence may be generated by the bulk shear instability and the wave troughs where the local shear can be enhanced to generate relatively weak turbulence.

a. Enhanced strong turbulent mixing

As explained in section 2, the threshold wind speed increases with height. Therefore, wind near the ground can readily exceed its threshold value, while wind speed higher up may not do so, often resulting in turbulent mixing decreasing with height. As a result of the decreasing influence of turbulence on the IGWs, the vertical velocity oscillation of the IGWs is more distinct at the upper levels of the 60-m observation layer (Figs. 5c, 8c, 11d), which is also clearly the case in Einaudi and Finnigan (1993) and Newsom and Banta (2003). A close examination of the major event on 20 October suggests that turbulent mixing is strong at the wave crests when the wind speed is enhanced by the presence of the IGWs, and the composite wind speed of the IGWs and the background flow at 0.5 m exceed the low-wind threshold for its low elevation (Fig. 11a). The strong turbulent mixing at the wave crests brings warm and high-momentum air downward. As a result, the air temperature is warmer at the wave crests than at the wave troughs, leading to a temperature oscillation, which is antiphase instead of in quadrature phase with the vertical velocity of the IGWs, and therefore a negative sensible heat flux at the wave frequency on both nights (Figs. 12, 13). Although both wind and temperature oscillations may be difficult to observe because of the wave–turbulence interactions that are embedded in the composite flow of the temporally varying background flow and the original IGWs, the covariances between $\tilde{w}$, $\tilde{V}$, and $\tilde{\theta}$ are clearly visible in the wavelet analysis (Figs. 12, 13).

The downward transfer of high-momentum air also enhances the wind speed at the wave crests observed at the lowest SA level. An example is the wind speed spike at 0.5 m around 0212 UTC 20 October (Fig. 11b); that is, the turbulent mixing enhances the amplitude of the IGWs near the ground. As the wind speed at the SA level exceeds its threshold value, the impact of the strong turbulence generated by the bulk shear instability on the background flow reaches 5 m first, as shown in the sharp drop of the 5-m wind speed (Fig. 11b). As the wind

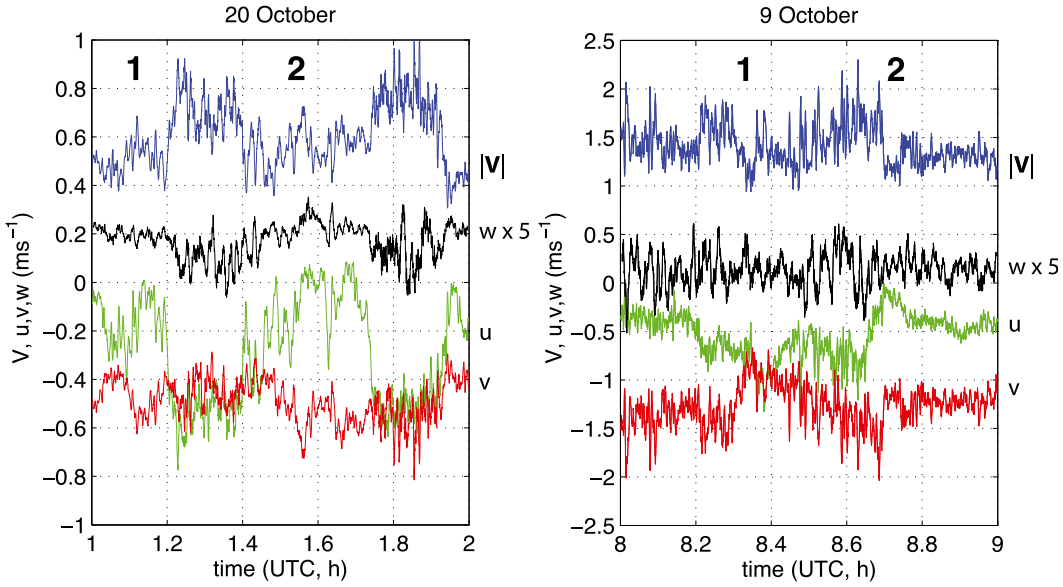

FIG. 9. The enlarged analysis of u (green), v (red), w (black), and V (blue) at the lowest SA level for the two minor cold currents (boldface 1 and 2) prior to the major cold current on each night, where V and w are approximately antiphase. The magnitude of w is enlarged 5 times for easy comparison.

speed at the SA level increases further, stronger turbulence is generated, and its impact on the background flow reaches 10 m, as shown in the sharp drop of the 10-m wind speed. The downward transfer of high-momentum air from 10 to 5 m can compensate for the momentum loss at 5 m through the momentum convergence, leading to a sudden wind speed increase or a local wind maximum at 5 m [i.e., a mini low-level jet (LLJ)], which is observed on both nights (Figs. 5f, 8f), as well as on 18 October during CASES-99 reported by Sun et al. (2004).

The strong turbulent mixing at the wave crests near the ground transports not only warm high-momentum air downward, but also cold low-momentum air upward. Consequently the wind speed and temperature at 5 m are lowered at the crests compared to the troughs (Fig. 11a), leading to the apparent reversed wavelike structure [i.e., the TFOs (section 2, Fig. 1)]. In other words, the TFOs at 5 m are forced by the strong turbulent mixing at the IGW wave crests. The wind and temperature of the TFOs are in phase at 5 m and are antiphase with the wind and temperature of the IGWs, leading to positive or countergradient wave fluxes at 5 m. As the vertical mixing generated by the bulk shear near the ground decreases with height, the influence of the low-momentum air near the ground on the upper air decreases with height. On 20 October, the countergradient wave fluxes are observed up to 30 m, but their magnitudes, on average, decrease with height. On 9 October, the IGWs are observed in the entire 60-m layer, and their amplitude is much larger compared to 20 October. Thus, the countergradient wave fluxes are observed only at 5 m as the turbulent mixing did not lower the wind speed at 10 m enough to reverse the wind speed oscillation there. The different depths of the TFO layer for the two nights suggest the dependence of the TFO depth on the strength of the vertical turbulent coupling and the amplitude of the IGWs. The strength of the strong turbulent mixing generated by the bulk shear is linearly proportional to wind speed, which implies that larger wave amplitude leads to stronger mixing. However, large-amplitude waves imply that the initial lifting is strong, which results in a deep IGW layer where the wind speed oscillation is also large at the upper level. For IGWs with large amplitude, the wind speed reduction at the upper mixing level may not be strong enough to reverse the phase of the wind speed oscillation there.

The in-phase relation between the horizontal and vertical components of the TFOs is not unique to the CASES-99 site. It is noticeable, for example, in the time series of horizontal and vertical velocities in Einaudi and Finnigan (1993). Countergradient wave heat fluxes have also been observed in the literature (e.g., Nai-Ping et al. 1983; Einaudi and Finnigan 1993), where turbulence is also thought to contribute to countergradient wave heat fluxes.

The mechanism of the TFOs is similar to the so-called Jeffreys's mechanism (Jeffreys 1925) used to explain the observed wave motion of water running down a sloped

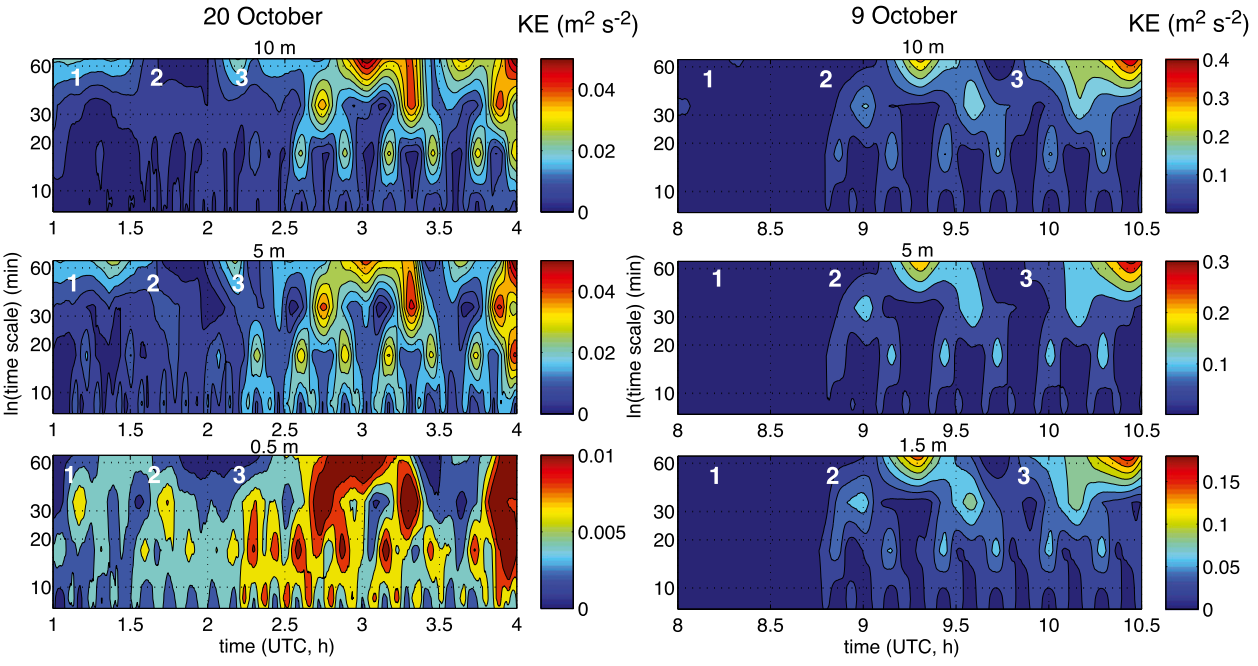

FIG. 10. The time–frequency distribution of $KE = 0.5(V^2 + w^2)$ using the Haar wavelet analysis at (top) 10 m, (middle) 5 m, and (bottom) the lowest SA level (0.5 m for 20 Oct and 1.5 m for 9 Oct) on (left) 20 Oct and (right) 9 Oct. The vertical axes are the log of the frequency time scale (min). The Haar wavelet analysis is performed for a time period of 2^{13} s at every 8 s. The numbers 1–3 are for the cold events for each night, as in Figs. 4 and 7. Note that the contour scale varies with height.

surface. Basically, Jeffreys's mechanism involves alternations between accelerated flow forced by the pressure gradient along the slope and decelerated flow due to the turbulent drag (Chimonas 1995; Pulido and Chimonas 2001; Chimonas 2003). Here, the reduction of wind speed by the vertical turbulent mixing and the acceleration of the airflow by the large-scale horizontal pressure gradient in the TFOs are analogous to Jeffreys's mechanism, while the IGWs are due to the exchange between kinetic and potential energy.

b. *Enhanced weak turbulent mixing*

In addition to the turbulence generated by the enhanced bulk shear instability at the wave crests, the IGWs at the lowest SA height also trigger turbulence through enhanced local shear at the wave troughs when the airspeed is low near the ground but relatively high above (Fig. 1). For example, the wind speed at 0.5 m is low at around 0224 UTC when the wind speed and the vertical velocity at 5 m are just recovered from their low values from the strong turbulent mixing at about 0215 UTC (Figs. 11a,c). Thus, the increased local shear between 0.5 and 5 m (marked with the dashed square at 0224 UTC in Fig. 11a) induces turbulent mixing between 0.5 and 5 m (Fig. 11c), which is visible in the high-frequency w oscillations at 0.5 and 5 m. A similar situation occurred around 0251 UTC (marked with the dashed square at 0251 UTC in Fig. 11a). When the horizontal variations of the second-moment terms can be assumed negligible, the momentum balance equations read (Garratt 1992),

$$\frac{d\overline{V}}{dt} = -\frac{\partial \overline{w'V'}}{\partial z} - \frac{1}{\overline{\rho}}\frac{\partial \overline{p}}{\partial x} \quad \text{and} \tag{2}$$

$$\frac{d\overline{w}}{dt} = -\frac{\partial \overline{w'w'}}{\partial z} - \frac{1}{\overline{\rho}}\frac{\partial \overline{p}}{\partial z} - g, \tag{3}$$

where $\overline{V}$, $\overline{w}$, $\overline{\rho}$, and $\overline{p}$ are the time-averaged horizontal wind speed and vertical motion, the air density, and air pressure. Because $\overline{w'w'} > 0$ and $\overline{w'V'} < 0$ as a result of the ground momentum sink, $\partial\overline{w'w'}/\partial z > 0$ and $\partial\overline{w'V'}/\partial z < 0$ if turbulent mixing increases with height. Assuming that the pressure gradients in (2) and (3) are time independent, the elevated turbulent mixing would lead to an increase in $\overline{V}$ and a decrease in $\overline{w}$. When this happens at the wave troughs of the near-ground IGWs, the increased wind speed would lead to an earlier appearance of the next wind speed oscillation (i.e., the wave period would be reduced). We call this new wave period the turbulence-reduced wave period. The observed turbulence-reduced wave period is visibly shorter after 0300 UTC, compared to its original value in Fig. 11a. The observed wave period reduction associated with turbulent

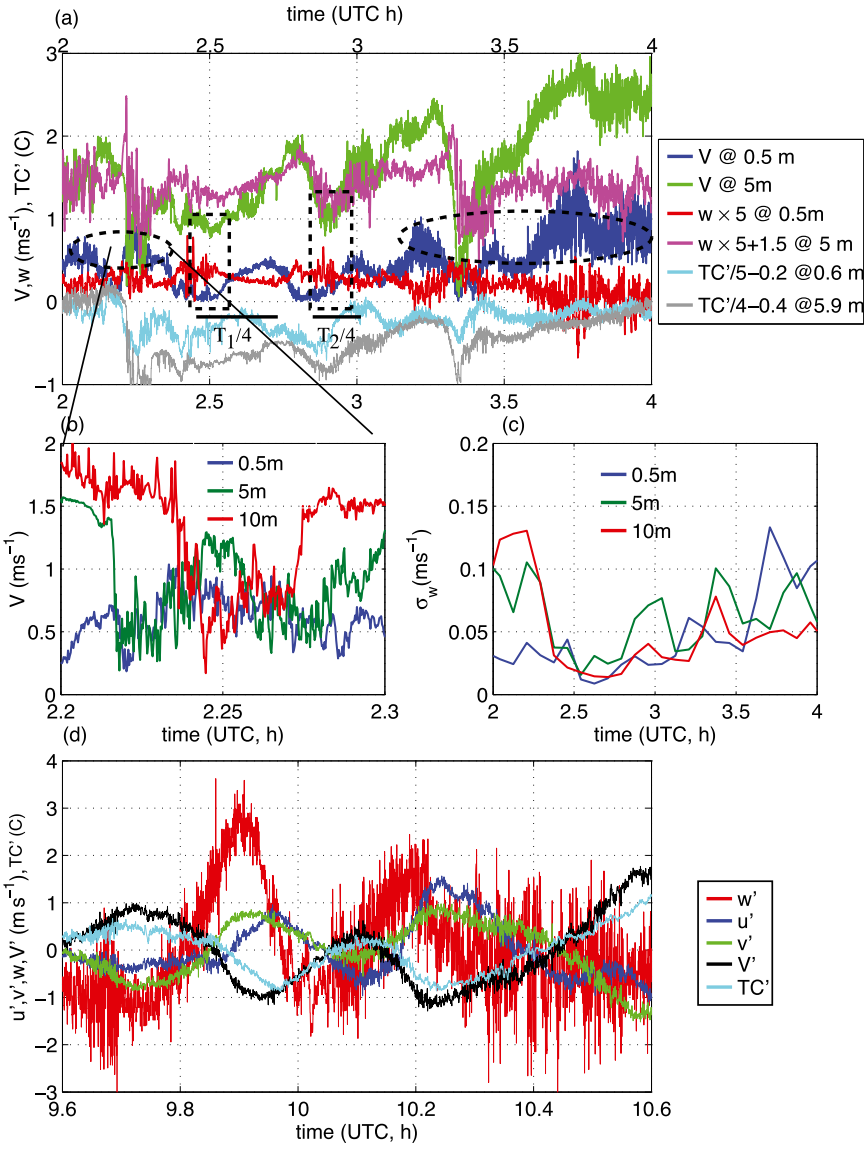

FIG. 11. (a)–(c) The zoomed-in time series of the major wave event on 20 Oct, and (d) the zoomed-in and linearly detrended (indicated by primes) time series of the major event at 55 m on 9 Oct, where V, u, v, w, and TC are the wind speed, the zonal, meridional, and vertical wind, and the thermocouple temperature, respectively. Shown in (b) is the zoomed-in V at the time of the first wind maximum at 0.5 m after the arrival of the cold current, indicating the formation of the mini LLJ as in Fig. 5f due to the strong turbulent mixing of large coherent eddies. In (a), the turbulence generated by the bulk shear instability and the local shear instability are marked with black dashed ellipses and rectangles, respectively; w is magnified, TC′ is reduced, and both are shifted for easy comparison; the wave periods for two cycles of the wind oscillations are also marked in (a), where T_2 is reduced by the elevated turbulent mixing at the wave trough at 0.5 m.

mixing is consistent with what Smith et al. (2007) found for mountain waves using a simple conceptual model.

c. *Observed turbulent mixing in relation to HOST and MOST*

In the above discussion, we qualitatively explain the wave–turbulence interactions based on the HOST concept of the different turbulent mixings in relation to wind speed. We now demonstrate how the turbulence strength as a function of wind speed during the wave–turbulence interaction period compares with the HOST in S12. Here we use the standard deviation of w, σ_w, over a 5-min period to represent the turbulence strength.

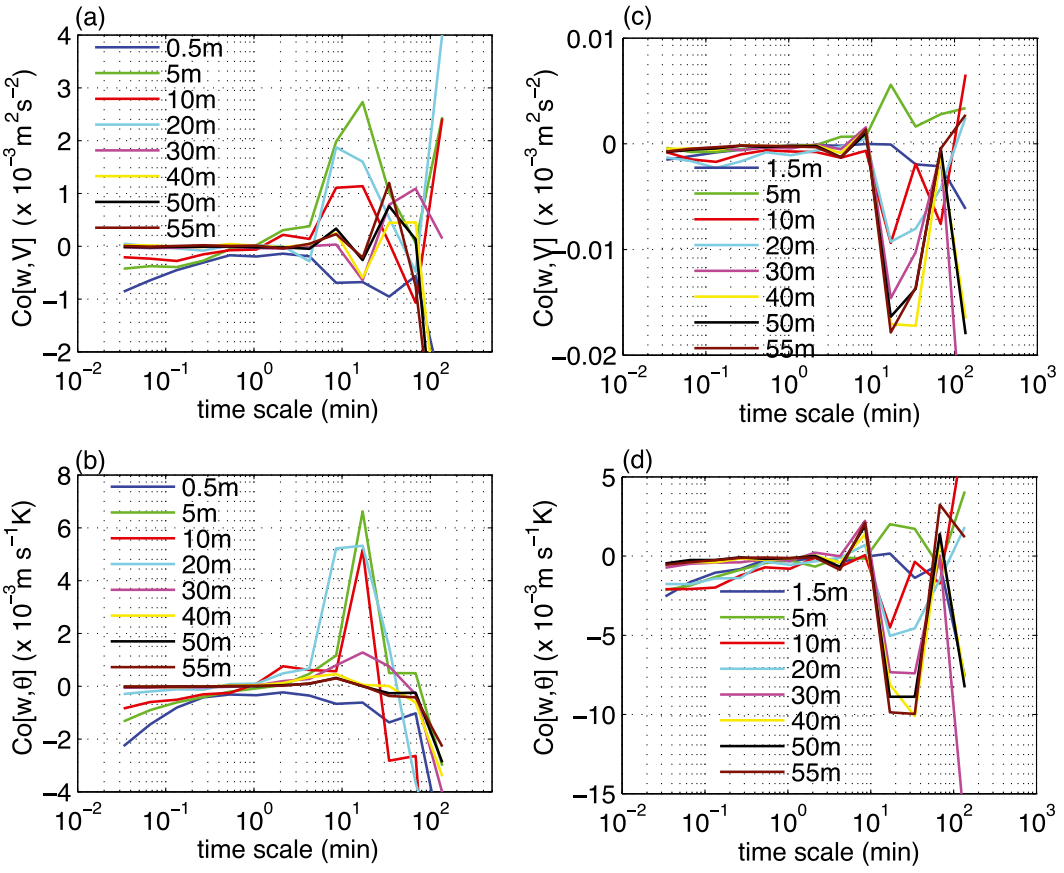

FIG. 12. The Haar wavelet cospectra (a),(c) between w and V and (b),(d) between w and θ on the nights of (a),(b) 20 Oct and of (c),(d) 9 Oct at the eight observation heights. The data segments used in the analysis, which are sampled at $1\,s^{-1}$, are between 0100 and 0600 UTC 20 Oct and between 0800 and 1200 UTC 9 Oct. The wind at each level is rotated to the vertically averaged wind direction for the time segment, which does not differ much if the wind is rotated to the time-averaged mean direction at each level.

In general, the observed σ_w variation with wind speed during the IGW periods, especially at the lowest SA levels (i.e., 0.5 m for 20 October and 1.5 m for 9 October), follows its variation averaged over all the nights during CASES-99 (Fig. 14). As the observation height increases to 5 m, some points deviate significantly from the averaged HOST at 5 m (Fig. 14a). A close examination indicates that some of the large deviations are due to a sharp decrease of both vertical and horizontal wind speeds within the 5-min-sampling segments as a result of a sudden increase of strong turbulent mixing below when the wind speed below exceeds its threshold value. In other words, the spikes of wind reduction within the 5-min segments result in large σ_w but small V (black triangles in Fig. 14). Some of the large deviations are due to the influence of the downward transport of strong turbulence from above as a result of a relatively weak LLJ around 50 m after 0400 UTC (Banta et al. 2007) when the wind speed at 5 m is still below the averaged threshold wind speed (magenta triangles in Fig. 14).

The general agreement between the two nights and σ_w averaged over the entire nocturnal CASES-99 periods as a function of V suggests that two turbulence regimes are common and consist of numerous weak and strong turbulent mixing events, which are either from the wave–turbulence interactions, as in the two nights investigated in this study, or periods of consistently low- or high-wind events. The large percentage of the relatively weak-background-wind nights during CASES-99 enables the frequent appearance of the wave–turbulence interactions like those observed in this study, which is confirmed by visual inspection of all the weak-wind nights during CASES-99.

In contrast to the relationship between σ_w and V, σ_w is related to $\partial V/\partial z$ only near the ground (i.e., at 0.5 and 1.5 m) because $V/z \sim \partial V/\partial z$ at those heights. At 5 m and above, σ_w is independent of $\partial V/\partial z$. Because relating

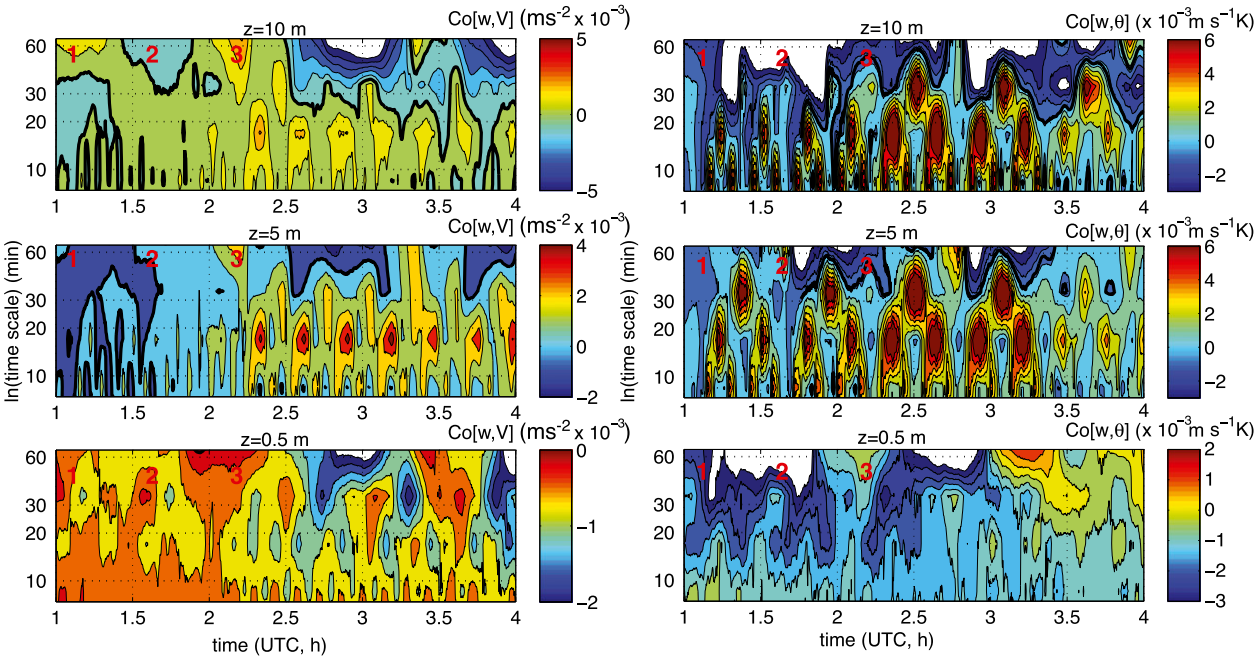

FIG. 13. The time–frequency Haar wavelet distribution of along-wind (left) momentum fluxes and (right) sensible heat fluxes at the lowest three SA levels for the night of 20 Oct. The thick black lines mark the zero value in each plot. The Haar wavelet analysis is performed for a time period of 2^{13} s at every 8 s. The vertical axes are the log of the frequency time scale (min). The red numbers 1–3 mark the cold events for the night, as in Fig. 4.

local vertical gradients to turbulent mixing is an essential assumption in MOST, the CASES-99 observations challenge the generality of MOST.

7. Conclusions

Using the unique CASES-99 dataset, we have investigated wave–turbulence interactions for two NBL cases using the HOST concept presented in S12. The observed wave–turbulence interactions, which are schematically summarized in Fig. 1, generate periodic patches of turbulence and turbulence-forced oscillations (TFOs) under weak winds.

The observed wavelike motions are buoyancy waves generated by uplifting as a result of the convergence between the background flow and surface cold currents in the NBL and are characterized by a typical IGW antiphase relationship between wind speed and vertical velocity. The cold currents can be drainage flows, but the most significant cold currents emanate from the cold pools in the surrounding gullies. We speculate that these relatively strong cold currents are the result of air cooling by vertical turbulent mixing over the cold pools.

The IGW wind oscillations near the ground trigger strong and vertically extended turbulent mixing at wave crests when the composite flow of the background flow and the wind speed oscillations exceeds the threshold wind speed at a given height and the bulk shear instability is triggered. The strong turbulence consists of large coherent eddies, which mix efficiently in the vertical direction. When the nocturnal air temperature increases significantly with height, these large eddies are capable of transporting the upper warm air downward and the near-ground cold air upward, which modifies the IGWs differently near the ground than at the upper level of the mixing depth. Near the ground, the downward-transported warm air results in temperature oscillations that are in phase with wind speed and approximately antiphase with the IGW vertical velocity, leading to a negative sensible heat flux at the IGW frequency. Heat transport at the observed IGW frequency would not exist without this wave–turbulence interaction. In addition, the strong turbulence also transports high-momentum air downward, which enhances the wind speed at the wave crests, leading to an apparent wave-amplitude increase.

In contrast, the strong turbulence mixing at the wave crests transports low-level air of relatively low momentum and temperature upward, leading to TFOs at the upper level of the mixing depth. These apparent waves have minimum wind speeds and temperature above the wave crests of the surface IGWs, resulting in a reversal of the wind speed and temperature oscillation compared to the IGWs near the ground. Therefore, both wave

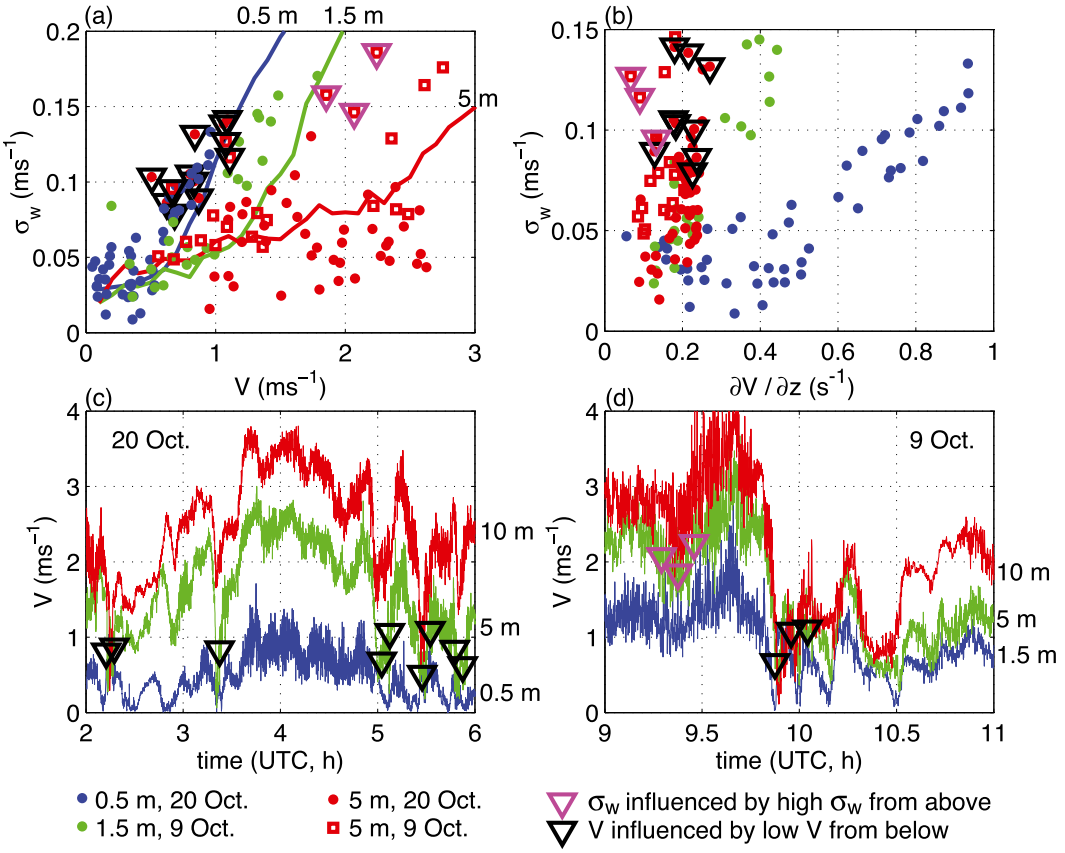

FIG. 14. (a) Relationships between V and σ_w at 0.5, 1.5, and 5 m, where the symbols are from the two nights (between 0200 and 0600 UTC 20 Oct and between 0900 and 1100 UTC 9 Oct) and the curves are the averaged relation during the entire nocturnal CASES-99 periods. (b) Relationship between $\partial V/\partial z$ and σ_w at the three levels. In addition, the time series of V at the lowest three SA levels are shown for the nights of (c) 20 Oct and (d) 9 Oct. Each symbol in (a) and (b) is a 5-min average. The black triangles mark those 5-min segments at 5 m that are affected by sharp decreases in both w and V because of the strong turbulent mixing below, as shown in (c) and (d). The magenta triangles mark those 5-min segments at 5 m influenced by the strong turbulent mixing from above and $V < V_s$. Note that the stronger wind at the higher level influences the vertical alignment of turbulent mixing.

momentum and heat fluxes of the TFOs are positive (i.e., countergradient). The depth of the TFO layer depends on the balance between the vertical extension of the turbulent mixing at the wave crests and the amplitude of the IGWs. We find that the reversed wind oscillations extend from 5 to 20 m on the night of 20 October when the IGW amplitude is relatively small, and they only exist at 5 m on the night of 9 October when the amplitude of the IGWs is relatively large and the IGWs are observed throughout the entire 60-m layer.

The relatively weak turbulent mixing is often generated by the enhanced local shear instability above the wave speed troughs when the wind speed near the ground is reduced while the wind speed above remains relatively large. The local shear has a finite vertical scale less than z but different from $\partial V/\partial z$. The relatively weak turbulent mixing generated by the local shear instability does not extend down to the ground and results in elevated turbulence patches detached from the surface. When turbulence increases with height over the wave troughs, the vertical transport of turbulent momentum decreases the mean vertical velocity but increases the mean wind speed, resulting in the apparent reduction in the wave period, or leading to the turbulence-reduced wave period.

Because the amplitudes of the IGWs or the TFOs are much larger than the turbulent fluctuations, and they are approximately either in phase or antiphase with the vertical velocity of the IGWs, the momentum and heat fluxes at the wave frequency are much larger than those at turbulence frequencies. Because of the wave–turbulence interaction and the temporal variation of the background flow, the wind and temperature oscillations may not be pure sine waves. In addition their coherence with the vertical velocity oscillation leads to significant momentum and heat transfer. Further investigation is needed to determine the generality of the result.

The consistency of the turbulence–wind relationship for the two cases considered here with the HOST concept in S12 suggests that this kind of wave–turbulence interaction, which is observed whenever the background wind is relatively weak, demonstrates the HOST concept documented in S12. Using the entire nocturnal dataset, we find that upward vertical velocity in general increases with decreasing wind speed when wind speed is weak during CASES-99 (not shown), which further suggests that wave generation from shallow cold currents may occur often. In addition, the consistent relationship between a negative meridional pressure gradient and weak southerly flow based on the entire CASES-99 dataset (Sun et al. 2013) suggests that the gullies south of the site may play an important role in generating relatively strong cold currents and IGWs. As the CASES-99 site is relatively flat compared to most of Earth's land surface, IGWs associated with cold pools and drainage flows are expected to be common in the NBL elsewhere, even though they may not always be easily identifiable, as their amplitude and period may vary with time as a result of wave–turbulence interactions.

Acknowledgments. The authors would like to acknowledge the field support from the Earth Observing Laboratory of the National Center for Atmospheric Research. We thank Bob Banta for his helpful comments and David Fitzjarrald and two anonymous reviewers for their critical reviews. The University Corporation for Atmospheric Research manages the National Center for Atmospheric Research under sponsorship by the National Science Foundation. Any opinions, findings and conclusions, or recommendations expressed in this publication are those of the authors and do not necessarily reflect the views of the National Science Foundation. Larry Mahrt was supported by the National Science Foundation through Grant AGS-1115011.

REFERENCES

Acevedo, O. C., and D. R. Fitzjarrald, 2003: In the core of the night—Effects of intermittent mixing on a horizontally heterogeneous surfaces. *Bound.-Layer Meteor.,* **106,** 1–33, doi:10.1023/A:1020824109575.

Balachandran, N. K., 1980: Gravity waves from thunderstorms. *Mon. Wea. Rev.,* **108,** 804–816, doi:10.1175/1520-0493(1980)108<0804:GWFT>2.0.CO;2.

Balsley, B., D. Fritts, R. Frehlich, R. M. Jones, S. Vadas, and R. Coulter, 2002: Up-gully flow in the great plains region: A mechanism for perturbing the nighttime lower atmosphere? *Geophys. Res. Lett.,* **29,** 1931, doi:10.1029/2002GL015435.

Banta, R. M., L. Mahrt, D. Vickers, J. Sun, B. B. Balsley, Y. L. Pichugina, and E. J. Williams, 2007: The very stable boundary layer on nights with weak low-level jets. *J. Atmos. Sci.,* **64,** 3068–3091, doi:10.1175/JAS4002.1.

Belcher, S. E., and N. Wood, 1996: Form and wave drag due to stably stratified turbulent flow over low ridges. *Quart. J. Roy. Meteor. Soc.,* **122,** 863–902, doi:10.1002/qj.49712253205.

——, I. N. Harman, and J. J. Finnigan, 2012: The wind in the willows: Flows in forest canopies in complex terrain. *Annu. Rev. Fluid Mech.,* **44,** 479–504, doi:10.1146/annurev-fluid-120710-101036.

Blumen, W., R. Banta, S. P. Burns, D. C. Fritts, R. Newsom, G. S. Poulos, and J. Sun, 2001: Turbulence statistics of a Kelvin–Helmholtz billow event observed in the night-time boundary layer during the Cooperative Atmosphere–Surface Exchange Study field program. *Dyn. Atmos. Oceans,* **34,** 189–204, doi:10.1016/S0377-0265(01)00067-7.

Brown, A. R., M. Athanassiadou, and N. Wood, 2003: Topographically induced waves within the stable boundary layer. *Quart. J. Roy. Meteor. Soc.,* **129,** 3357–3370, doi:10.1256/qj.02.176.

Carpenter, J. R., E. W. Tedford, E. Heifetz, and G. A. Lawrence, 2013: Instability in stratified shear flow: Review of a physical interpretation based on interacting waves. *Appl. Mech. Rev.,* **64,** 060801, doi:10.1115/1.4007909.

Chemel, C., C. Staquet, and Y. Largeron, 2009: Generation of internal gravity waves by a katabatic wind in an idealized alpine valley. *Meteor. Atmos. Phys.,* **103,** 187–194, doi:10.1007/s00703-009-0349-4.

Chilson, P. B., A. Muschinski, and G. Schmidt, 1997: First observations of Kelvin–Helmholtz billows in an upper level jet stream using VHF frequency domain interferometry. *Radio Sci.,* **32,** 1149–1160, doi:10.1029/97RS00088.

Chimonas, G., 1995: Long-wavelength gravity wave instabilities: A comparison of the Jeffreys drag mechanism with the shear instability. *J. Atmos. Sci.,* **52,** 191–195, doi:10.1175/1520-0469(1995)052<0191:LWGWIA>2.0.CO;2.

——, 2002: On internal gravity waves associated with the stable boundary layer. *Bound.-Layer Meteor.,* **102,** 139–155, doi:10.1023/A:1012730306799.

——, 2003: Pressure gradient amplification of shear instabilities in the boundary layer. *Dyn. Atmos. Oceans,* **37,** 131–145, doi:10.1016/S0377-0265(03)00028-9.

——, and C. J. Nappo, 1987: A thunderstorm bow wave. *J. Atmos. Sci.,* **44,** 533–541, doi:10.1175/1520-0469(1987)044<0533:ATBW>2.0.CO;2.

——, and ——, 1989: Wave drag in the planetary boundary layer over complex terrain. *Bound.-Layer Meteor.,* **47,** 217–232, doi:10.1007/BF00122330.

Costa, F. D., O. C. Acevedo, J. C. M. Mombach, and G. A. Degrazia, 2011: A simplified model for intermittent turbulence in the nocturnal boundary layer. *J. Atmos. Sci.,* **68,** 1714–1729, doi:10.1175/2011JAS3655.1.

Coulter, R., and J. Doran, 2002: Spatial and temporal occurrences of intermittent turbulence during CASES-99. *Bound.-Layer Meteor.,* **105,** 329–349, doi:10.1023/A:1019993703820.

Curry, M. J., and R. C. Murty, 1974: Thunderstorm-generated gravity waves. *J. Atmos. Sci.,* **31,** 1402–1408, doi:10.1175/1520-0469(1974)031<1402:TGGW>2.0.CO;2.

Doran, J. C., 2004: Characteristics of intermittent turbulent temperature fluxes in stable conditions. *Bound.-Layer Meteor.,* **112,** 241–255, doi:10.1023/B:BOUN.0000027907.06649.d0.

Dörnbrack, A., and C. J. Nappo, 1997: A note on the application of linear wave theory at a critical level. *Bound.-Layer Meteor.,* **82,** 399–416, doi:10.1023/A:1000270821161.

Einaudi, F., and J. J. Finnigan, 1981: The interaction between an internal gravity wave and the planetary boundary layer. Part I:

the linear analysis. *Quart. J. Roy. Meteor. Soc.,* **107,** 793–806, doi:10.1002/qj.49710745404.

——, and ——, 1993: Wave–turbulence dynamics in the stably stratified boundary layer. *J. Atmos. Sci.,* **50,** 1841–1864, doi:10.1175/1520-0469(1993)050<1841:WTDITS>2.0.CO;2.

——, A. J. Bedard Jr., and J. J. Finnigan, 1989: A climatology of gravity waves and other coherent disturbances at the Boulder Atmospheric Observatory during March–April 1984. *J. Atmos. Sci.,* **46,** 303–329, doi:10.1175/1520-0469(1989)046<0303:ACOGWA>2.0.CO;2.

Finnigan, J. J., and F. Einaudi, 1981: The interaction between an internal gravity wave and the planetary boundary layer. Part II: Effect of the wave on the turbulence structure. *Quart. J. Roy. Meteor. Soc.,* **107,** 807–832, doi:10.1002/qj.49710745405.

——, ——, and D. Fua, 1984: The interaction between an internal gravity wave and turbulence in the stably-stratified nocturnal boundary layer. *J. Atmos. Sci.,* **41,** 2409–2436, doi:10.1175/1520-0469(1984)041<2409:TIBAIG>2.0.CO;2.

——, R. H. Shaw, and E. G. Patton, 2009: Turbulence structure above a vegetation canopy. *J. Fluid Mech.,* **637,** 387–424, doi:10.1017/S0022112009990589.

Fitzjarrald, D. R., and K. E. Moore, 1990: Mechanisms of nocturnal exchange between the rain forest and the atmosphere. *J. Geophys. Res.,* **95,** 16 839–16 850, doi:10.1029/JD095iD10p16839.

Fritts, D. C., C. Nappo, D. M. Riggin, B. B. Balsley, W. E. Eichinger, and R. K. Newsom, 2003: Analysis of ducted motions in the stable nocturnal boundary layer during CASES-99. *J. Atmos. Sci.,* **60,** 2450–2471, doi:10.1175/1520-0469(2003)060<2450:AODMIT>2.0.CO;2.

Garratt, J. R., 1992: *The Atmospheric Boundary Layer.* Cambridge Atmospheric and Space Science Series, Cambridge University Press, 316 pp.

Geller, M. A., H. Tanaka, and D. C. Fritts, 1975: Production of turbulence in the vicinity of critical levels for internal gravity waves. *J. Atmos. Sci.,* **32,** 2125–2135, doi:10.1175/1520-0469(1975)032<2125:POTITV>2.0.CO;2.

Gossard, E. E., and W. H. Hooke, 1975: *Waves in the Atmosphere: Atmospheric Infrasound and Gravity Waves. Their Generation and Propagation.* Elsevier Scientific Publishing Company, 456 pp.

——, J. E. Gaynor, R. J. Zamora, and W. D. Neff, 1985: Finestructure of elevated stable layers observed by sounder and *in situ* tower sensors. *J. Atmos. Sci.,* **42,** 2156–2169, doi:10.1175/1520-0469(1985)042<2156:FOESLO>2.0.CO;2.

Ha, K.-J., Y.-K. Hyun, H.-M. Oh, K.-E. Kim, and L. Mahrt, 2007: Evaluation of boundary layer similarity theory for stable conditions in CASES-99. *Mon. Wea. Rev.,* **135,** 3474–3483, doi:10.1175/MWR3488.1.

Hardy, K. R., R. J. Reed, and G. K. Mather, 1973: Observation of Kelvin–Helmholtz billows and their mesoscale environment by radar, instrumented aircraft, and a dense radiosonde network. *Quart. J. Roy. Meteor. Soc.,* **99,** 279–293, doi:10.1002/qj.49709942007.

Howell, J., 1995: Identifying sudden changes in data. *Mon. Wea. Rev.,* **123,** 1207–1212, doi:10.1175/1520-0493(1995)123<1207:ISCID>2.0.CO;2.

——, and L. Mahrt, 1994: An adaptive multiresolution data filter: Applications to turbulence and climatic time series. *J. Atmos. Sci.,* **51,** 2165–2178, doi:10.1175/1520-0469(1994)051<2165:AAMDFA>2.0.CO;2.

——, and J. Sun, 1999: Surface-layer fluxes in stable conditions. *Bound.-Layer Meteor.,* **90,** 495–520, doi:10.1023/A:1001788515355.

Hu, X., X. Lee, D. E. Stevens, and R. B. Smith, 2002: A numerical study of nocturnal wavelike motion in forests. *Bound.-Layer Meteor.,* **102,** 199–223, doi:10.1023/A:1013167228992.

Jeffreys, H., 1925: The flow of water in an inclined channel of rectangular section. *Philos. Mag.,* **49,** 793–807, doi:10.1080/14786442508634662.

Jordan, A. R., 1972: Atmospheric gravity waves from winds and storms. *J. Atmos. Sci.,* **29,** 445–456, doi:10.1175/1520-0469(1972)029<0445:AGWFWA>2.0.CO;2.

King, J. C., S. D. Mobbs, and N. R. Edwards, 1994: Surface boundary conditions in stably-stratified environmental flows. *Stably Stratified Flows: Flow and Dispersion over Topography,* I. P. Castro and N. J. Rockliff, Eds., Institute of Mathematics and Its Applications Conf. Series, Vol. 52, Oxford University Press, 93–103.

Kunkel, K. E., and D. L. Walters, 1982: Intermittent turbulence in measurements of the temperature structure parameter under very stable conditions. *Bound.-Layer Meteor.,* **22,** 49–60, doi:10.1007/BF00128055.

Lee, X., H. H. Neumann, G. D. Hartog, J. D. Fuentes, T. A. Black, R. E. Mickle, P. C. Yang, and P. D. Blaken, 1997: Observation of gravity waves in a boreal forest. *Bound.-Layer Meteor.,* **84,** 383–398, doi:10.1023/A:1000454030493.

Lenschow, D., B. Stankov, and L. Mahrt, 1979: The rapid morning boundary-layer transition. *J. Atmos. Sci.,* **36,** 2108–2124, doi:10.1175/1520-0469(1979)036<2108:TRMBLT>2.0.CO;2.

Mahrt, L., 1989: Intermittency of atmospheric turbulence. *J. Atmos. Sci.,* **46,** 79–95, doi:10.1175/1520-0469(1989)046<0079:IOAT>2.0.CO;2.

——, 2010: Common microfronts and other solitary events in the nocturnal boundary layer. *Quart. J. Roy. Meteor. Soc.,* **136,** 1712–1722, doi:10.1002/qj.694.

——, C. Thomas, S. Richardson, N. Seaman, D. Stauffer, and M. Zeeman, 2013: Non-stationary generation of weak turbulence for very stable and weak-wind conditions. *Bound.-Layer Meteor.,* **147,** 179–199, doi:10.1007/s10546-012-9782-x.

Mann, M. E., R. S. Bradley, and M. K. Hughes, 1999: Northern hemisphere temperatures during the past millennium: Inferences, uncertainties, and limitations. *Geophys. Res. Lett.,* **26,** 759–762, doi:10.1029/1999GL900070.

Martins, H. S., L. D. A. Sá, and O. L. L. Moraes, 2013: Low level jets in the Pantanal wetland nocturnal boundary layer—Case studies. *Amer. J. Environ. Eng.,* **3,** 32–47, doi:10.5923/j.ajee.20130301.06.

Meillier, Y. P., R. G. Frehlich, R. M. Jones, and B. B. Balsley, 2008: Modulation of small-scale turbulence by ducted gravity waves in the nocturnal boundary layer. *J. Atmos. Sci.,* **65,** 1414–1427, doi:10.1175/2007JAS2359.1.

Nai-Ping, L., W. D. Neff, and J. C. Kaimal, 1983: Wave and turbulence structure in a disturbed nocturnal inversion. *Bound.-Layer Meteor.,* **26,** 141–155, doi:10.1007/BF00121539.

Nappo, C. J., 1991: Sporadic breakdowns of stability in the PBL over simple and complex terrain. *Bound.-Layer Meteor.,* **54,** 69–87, doi:10.1007/BF00119413.

——, 2012: *An Introduction to Atmospheric Gravity Waves.* 2nd ed. International Geophysics Series, Vol. 102, Academic Press, 400 pp.

——, and G. Chimonas, 1992: Wave exchange between the ground surface and a boundary-layer critical level. *J. Atmos. Sci.,* **49,** 1075–1091, doi:10.1175/1520-0469(1992)049<1075:WEBTGS>2.0.CO;2.

——, D. R. Miller, and A. L. Hiscox, 2008: Wave-modified flux and plume dispersion in the stable boundary layer. *Bound.-Layer Meteor.,* **129,** 211–223, doi:10.1007/s10546-008-9315-9.

Newsom, R. K., and R. M. Banta, 2003: Shear-flow instability in the stable nocturnal boundary layer as observed by Doppler lidar during CASES-99. *J. Atmos. Sci.,* **60,** 16–33, doi:10.1175/1520-0469(2003)060<0016:SFIITS>2.0.CO;2.

Poulos, G. S., and Coauthors, 2002: CASES-99: A comprehensive investigation of the stable nocturnal boundary layer. *Bull. Amer. Meteor. Soc.,* **83,** 555–581, doi:10.1175/1520-0477(2002)083<0555:CACIOT>2.3.CO;2.

Pulido, M., and G. Chimonas, 2001: Forest canopy waves: The long-wavelength component. *Bound.-Layer Meteor.,* **100,** 209–224, doi:10.1023/A:1019246513260.

Rees, J. M., and S. D. Mobbs, 1988: Studies of internal gravity waves at Halley Base, Antarctica, using wind observations. *Quart. J. Roy. Meteor. Soc.,* **114,** 939–966, doi:10.1002/qj.49711448206.

——, and J. W. Rottman, 1994: Analysis of solitary disturbances over an Antarctic Ice Shelf. *Bound.-Layer Meteor.,* **69,** 285–310, doi:10.1007/BF00708859.

——, J. C. W. Denholm-Price, J. C. King, and P. S. Anderson, 2000: A climatological study of internal gravity waves in the atmospheric boundary layer overlying the Brunt Ice Shelf, Antarctica. *J. Atmos. Sci.,* **57,** 511–526, doi:10.1175/1520-0469(2000)057<0511:ACSOIG>2.0.CO;2.

——, W. J. Staszewski, and J. R. Winkler, 2001: Case study of a wave event in the stable atmospheric boundary layer overlying an Antarctic Ice Shelf using the orthogonal wavelet transform. *Dyn. Atmos. Oceans,* **34,** 245–261, doi:10.1016/S0377-0265(01)00070-7.

Smith, R. B., 1989: Hydrostatic airflow over mountains. *Advances in Geophysics,* Vol. 31, Academic Press, 1–41.

——, J. D. Doyle, Q. Jiang, and S. A. Smith, 2007: Alpine gravity waves: Lessons from MAP regarding mountain wave generation and breaking. *Quart. J. Roy. Meteor. Soc.,* **133,** 917–936, doi:10.1002/qj.103.

Soler, M. R., C. Infante, P. Buenestado, and L. Mahrt, 2002: Observations of nocturnal drainage flow in a shallow gully. *Bound.-Layer Meteor.,* **105,** 253–273, doi:10.1023/A:1019910622806.

Staquet, C., 2004: Gravity and inertia-gravity internal waves: Breaking processes and induced mixing. *Surv. Geophys.,* **25,** 281–314, doi:10.1007/s10712-003-1280-8.

——, and J. Sommeria, 2002: Internal gravity waves: From instabilities to turbulence. *Annu. Rev. Fluid Mech.,* **34,** 559–593, doi:10.1146/annurev.fluid.34.090601.130953.

Sun, J., 2011: Vertical variations of the mixing lengths under neutral and stable conditions during CASES-99. *J. Appl. Meteor. Climatol.,* **50,** 2030–2041, doi:10.1175/JAMC-D-10-05006.1.

——, and S. F. De Wekker, 2012: Atmospheric carbon dioxide transport over mountainous terrain. *Mountain Ecosystems: Dynamics, Management and Conservation,* K. E. Richards, Ed., Nova Science Publishers, 101–121.

——, and Coauthors, 2002: Intermittent turbulence associated with a density current passage in the stable boundary layer. *Bound.-Layer Meteor.,* **105,** 199–219, doi:10.1023/A:1019969131774.

——, and Coauthors, 2004: Atmospheric disturbances that generate intermittent turbulence in nocturnal boundary layers. *Bound.-Layer Meteor.,* **110,** 255–279, doi:10.1023/A:1026097926169.

——, L. Mahrt, R. M. Banta, and Y. L. Pichugina, 2012: Turbulence regimes and turbulence intermittency in the stable boundary layer during CASES-99. *J. Atmos. Sci.,* **69,** 338–351, doi:10.1175/JAS-D-11-082.1.

——, D. H. Lenschow, L. Mahrt, and C. J. Nappo, 2013: The relationships among wind, horizontal pressure gradient, and turbulent momentum transport during CASES-99. *J. Atmos. Sci.,* **70,** 3397–3414, doi:10.1175/JAS-D-12-0233.1.

Teixeira, M. A. C., and P. M. A. Miranda, 2004: The effect of wind shear and curvature on the gravity wave drag produced by a ridge. *J. Atmos. Sci.,* **61,** 2638–2643, doi:10.1175/JAS3282.1.

Thorpe, S. A., 1987: Transitional phenomena and the development of turbulence in stratified fluids: A review. *J. Geophys. Res.,* **92,** 5231–5248, doi:10.1029/JC092iC05p05231.

Tjernström, M., B. B. Balsley, G. Svensson, and C. J. Nappo, 2009: The effects of critical layers on residual layer turbulence. *J. Atmos. Sci.,* **66,** 468–480, doi:10.1175/2008JAS2729.1.

van de Wiel, B. J. H., A. F. Moene, O. K. Hartogensis, H. A. R. De Bruin, and A. A. M. Holtslag, 2003: Intermittent turbulence in the stable boundary layer over land. Part III: A classification for observations during CASES-99. *J. Atmos. Sci.,* **60,** 2509–2522, doi:10.1175/1520-0469(2003)060<2509:ITITSB>2.0.CO;2.

——, ——, H. J. J. Jonker, P. Baas, S. Basu, J. M. M. Donda, J. Sun, and A. A. M. Holtslag, 2012: The minimum wind speed for sustainable turbulence in the nocturnal boundary layer. *J. Atmos. Sci.,* **69,** 3116–3127, doi:10.1175/JAS-D-12-0107.1.

Viana, S., E. Terradellas, and C. Yagüe, 2010: Analysis of gravity waves generated at the top of a drainage flow. *J. Atmos. Sci.,* **67,** 3949–3966, doi:10.1175/2010JAS3508.1.

Vindel, J., and C. Yagüe, 2011: Intermittency of turbulence in the atmospheric boundary layer: Scaling exponents and stratification influence. *Bound.-Layer Meteor.,* **140,** 73–85, doi:10.1007/s10546-011-9597-1.

Vosper, S. B., and A. R. Brown, 2007: The effect of small-scale hills on orographic drag. *Quart. J. Roy. Meteor. Soc.,* **133,** 1345–1352, doi:10.1002/qj.101.

Yagüe, C., G. Maqueda, and J. M. Rees, 2001: Characteristics of turbulence in the lower atmosphere at Halley IV station, Antarctica. *Dyn. Atmos. Oceans,* **34,** 205–223, doi:10.1016/S0377-0265(01)00068-9.

Zhou, B., and F. K. Chow, 2012: Turbulence modeling for the stable atmospheric boundary layer and implications for wind energy. *Flow Turbul. Combust.,* **88,** 255–277, doi:10.1007/s10494-011-9359-7.

——, and ——, 2014: Nested large-eddy simulations of the intermittently turbulent stable atmospheric boundary layer over real terrain. *J. Atmos. Sci.,* **71,** 1021–1039, doi:10.1175/JAS-D-13-0168.1.